



Technische
Universität
München



Walther-Meißner
Institut



Bayerische
Akademie
der Wissenschaften

Scanning Tunneling Microscopy and Raman Spectroscopy in 1T-TaSe₂

Master's Thesis
Minghao Zhang

Supervisor: Prof. Dr. Rudi Hackl
Garching, May 2021



TECHNISCHE UNIVERSITÄT MÜNCHEN

Contents

1	Introduction	1
2	Principles	4
2.1	Principles of Scanning tunneling microscopy	4
2.2	Principles of Raman scattering	9
3	Setup	12
3.1	Scanning tunneling microscopy	12
3.2	Raman spectroscopy	15
3.2.1	Optical path	15
3.2.2	Focusing and alignment procedure	16
3.2.3	Measurement with Raman spectroscopy	17
3.3	Tip fabrication	18
4	Measurement	22
4.1	STM experiment	22
4.1.1	Noise spectrum	22
4.1.2	Parameters setting of the Attocube software	23
4.1.3	STM measurement on amorphous gold	23
4.1.4	STM measurement on Au(111)	26
4.1.5	STM measurement on 1T-TaSe ₂	27
4.2	Raman measurement	28
4.2.1	Raman spectra of Si(110)	28
4.2.2	Raman measurement on 1T-TaSe ₂	29

5	The upgrade and mounting of the TERS set-up	37
5.1	The new design and mounting process of TERS set-up	37
5.2	Tests on the new set-up	39
6	Summary	43
7	Bibliography	45
8	Acknowledgement	49

1 Introduction

The frontiers of condensed matter physics research are often focused on the low-energy excited states of electrons. In the case of superconductivity, for example, the typical energy excitation scale is of the order of meV. In order to study these low-energy excited states, scientists have developed a large number of spectroscopic measurements such as STM (Scanning Tunnelling Microscopy) [1, 2], ARPES (Angle-resolved photoemission spectroscopy) [3], Neutron diffraction [4], XRD (X-ray powder diffraction) [5], Infrared and Raman Spectroscopies [6], RIXS (Resonant inelastic X-ray scattering) [7]. Modern spectroscopic tools are divided into two main categories: single-particle spectroscopy, which studies the behaviour of single-particle excitations, such as STM, ARPES, and two-particle spectroscopies, such as Raman, RIXS (Resonant inelastic X-ray scattering). The two types of methods are complementary and sensitive to different types of excitations. In systems with strong electronic correlations the differences in the spectral features encode the type of correlations.

Since its invention in 1981 by the German scientist G. Binnig and the Swiss scientist Heinrich Rohrer [8], at their laboratory in Zurich, Switzerland, STM has become well-known for its supreme imaging resolution. The STM allowed us for the first time to observe information on the surface of a sample in real time with atomic-level resolution, for which the two scientists, together with Ernst Ruska, the inventor of the electron microscope, shared the Nobel Prize in Physics in 1986 [9].

The primary function of Scanning Tunneling Microscopy is to get topographical mappings of surfaces. In using an STM, there has to be a tip rastered across the surface and maintained between the sample and the tip by making adjustments of the height's tip. When displayed through various positions and measurements, the tip's height plot displays the full dimensions of the required topographical features, obtaining information that has been atomically resolved on semiconducting and metallic surfaces.

In the last decade, STM has made great achievements in atomic and molecular observation, modification and processing in a wide range of disciplines such as physics, chemistry and biology [10].

The Raman effect is a type of inelastic scattering of visible light arising from practically all excitations

in matter, specifically solids including the vibrations of molecules and lattices. It was theoretically predicted by A. Smekal in 1923 and was first observed in liquids by the Indian scientists C. V. Raman and K. S. Krishnan in 1928 [11, 12]. Shortly after Raman and Krishnan's article, Landberg and Manderstam reported in Russia that they had observed light scattering in quartz with a change in frequency. Before the 1960s, the application of Raman scattering was limited by the low energy density and poor monochromaticity of the light sources, but after the 1960s, with the use of lasers, Raman scattering has become more widely used [13]. Raman scattering is accompanied by an exchange of energy and a change in the frequency of the light waves before and after scattering. The analysis of the energy difference before and after scattering gives information about the electronic, magnetic and lattice properties of a material, which is of great practical value.

In 1955, Peierls pointed out that one-dimensional metal atomic chains are unstable at low temperatures due to electron-phonon interactions, which will distort the lattice with periodic modulation of the charge density, the charge density wave (CDW) [14].

Two-dimensional metallic transition metal dichalcogenides (TMDs) are of interest for studying phenomena such as charge-density wave (CDW) and superconductivity. Tantalum diselenide (1T-TaSe₂) are typical metallic TMDs exhibiting rich CDW phase transitions [15, 16].

The bulk 1T-TaSe₂ transitions from normal state to incommensurate CDW state below 600K and into commensurate CDW state below 473K [17]. During the I-CDW to C-CDW phase transition, the CDW supercell undergoes a $\sqrt{13} \times \sqrt{13}$ reconstruction in which the basal-plane lattice vectors increase by $\sqrt{13}$ and rotate by 13.9° with respect to the original lattice vectors [18, 19].

For a comprehensive study of CDW materials, the Raman spectroscopy alone is not sufficient for the research. If STM and Raman spectroscopy are used in conjunction of each other, the spatial resolution is improved and the Raman signal can be observed as well in different regions. STM has a very high spatial resolution, but it is not possible to observe phonons. By studying phonons, we can obtain some indications of the distortion of the lattice structure in the sample. Using the two technologies together, the systems with lattice distortions in the CDW phase can be studied in greater detail [20]. Although there are many studies on Raman or STM for TMD materials, studies on the combination of Raman spectroscopy and STM for 1T-TaSe₂ are still lacking.

For this work, Raman scattering and STM measurements have been performed on the CDW material 1T-TaSe₂. The basic principles of the Raman scattering and STM are presented in chapter 2. In chapter

3, the experimental setup is described. The results of the measurements on 1T-TaSe₂ are presented and discussed in chapter 4. Chapter 5 introduces the upgrade and mounting of the custom, lab-built TERS set-up. Chapter 6 finally gives a conclusion of the work done in regard of this thesis.

2 Principles

2.1 Principles of Scanning tunneling microscopy

STM operates under the principle of quantum mechanical tunneling effect. This microscopy technique allows us to obtain atomic-level real space images of conducting surfaces [21]. The probability of electron tunneling through a typical potential barrier depends on the width of the potential barrier, which will be discussed in detail in this section. The following paragraphs are almost literally taken from [22].

The quantum tunneling effect is the basic working principle of STM. Quantum mechanics describes microscopic particles with fluctuations that pass with a certain probability through a potential barrier above their energy [23]. If a classical potential barrier separates two conductors (e.g. a vacuum or an insulating oxide layer), it is possible for electrons to tunnel from one conductor to the other. Consider a one-dimensional model of a square potential barrier with potential energy $U(z)$ and solve the Schrodinger equation in the potential barrier region:

$$-\frac{\hbar^2}{2m} \frac{\partial^2 \psi_n(z)}{\partial z^2} + U(z)\psi_n(z) = E\psi_n(z) \quad (2.1)$$

where \hbar is the reduced Planck constant, z is the position of the electron, and m is the mass of the electron [22]. The solution for an electron in the classical propagating region ($E > U$) has the following expression:

$$\psi_n(z) = \psi_n(0)e^{\pm ikz} \quad (2.2)$$

Here,

$$k = \sqrt{2m(E - U)}/\hbar, \quad (2.3)$$

the corresponding electrons have constant momentum $p_z = \hbar k$, which is consistent with the classical case. If the position of the electron is in the classically forbidden region ($E < U$), the solution of the

wave function is a decay function:

$$\psi_n(z) = \psi_n(0)e^{\pm\kappa z} \quad (2.4)$$

Here,

$$\kappa = \sqrt{2m(U - E)}/\hbar, \quad (2.5)$$

represents the degree of attenuation of the wave function within the potential barrier.

The above solution indicates that the electron has a certain probability of penetrating the potential barrier to reach the other side of the barrier, which is a manifestation of the quantum tunneling effect. Based on the wave function we can calculate the probability of an electron appearing at any position. When the tip of the scanning tunneling microscope is close enough to the sample, electrons on one side of the tip may appear on the sample side, and vice versa. Assuming that the distance between the sample and tip is d , the probability of finding electrons from the $\psi_n(z)$ state of the tip on the sample side is:

$$p \propto |\psi_n(0)|^2 e^{-2\kappa d} \quad (2.6)$$

Therefore the probability that an electron in the eV energy range near the Fermi surface will be present in the sample as:

$$p \propto \sum_{E_f - eV}^{E_f} |\psi_n(0)|^2 e^{-2\kappa d} \equiv \rho(E) \cdot eV \quad (2.7)$$

where E_f is the Fermi energy of electrons. The tunneling current is determined by the total number of all possible states in the energy interval $E_f - eV$ per volume-unit momentum space, and the tunneling current is determined by it. The above equation uses the expression for the density of states near the Fermi surface with energy E as:

$$\rho_s(z, E) = \frac{1}{\epsilon} \sum_{E-\epsilon}^E |\psi_n(z)|^2 \quad (2.8)$$

Therefore, the probability of electron tunneling within the energy eV interval near the Fermi surface is proportional to the density of states near the Fermi surface. The $e^{-2\kappa d}$ term is the basis for the longitudinal resolution of the STM.

In order to form a stable tunneling current, several additional conditions need to be met [24]. The first is that the electron hopping rule is satisfied, which means that under the condition that the tip wave function overlaps with the sample wave function, electrons can only hop from the electron-occupied state of the tip to the electron-unoccupied state permitted by the sample, or conversely, from the

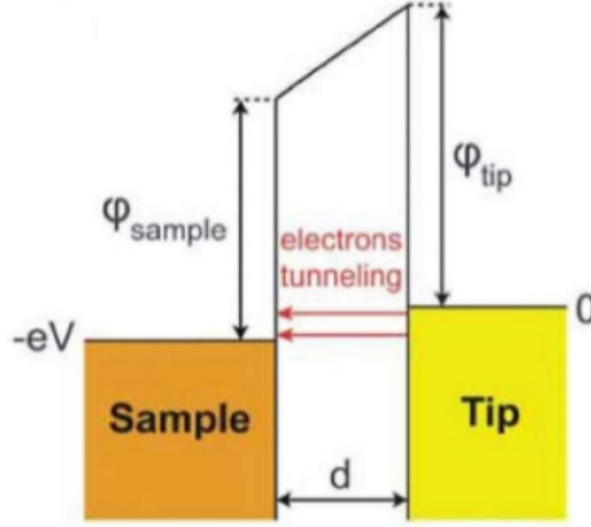


Figure 2.1: Tunneling effect under a vacuum potential barrier [22].

sample-occupied state to the permitted tip unoccupied state. According to Fermi's Golden Rule, the hopping probability is determined by the hopping matrix element M . In addition the electron obeys Fermi-Dirac statistical law, and the probability of an electron occupying an electronic state with energy E is:

$$f(E) = 1/\{1 + [\exp(E - E_f)/k_B T]\} \quad (2.9)$$

Secondly, a voltage needs to be applied between the sample and the tip in order to produce unequal electron tunneling probabilities on both sides. The total tunneling current can be therefore as:

$$I = \frac{4\pi e^2}{\hbar} \int_{-\infty}^{+\infty} |M|^2 [f(E_F - eV + \epsilon) - f(E_F + \epsilon)] \rho_s(E_F - eV + \epsilon) \rho_t(E_F + \epsilon) d\epsilon \quad (2.10)$$

where the tunneling matrix element is an Elements of Bardeen matrix, which can be written as:

$$M = \frac{\hbar}{2m} \int (\chi^* \frac{\partial \psi}{\partial z} - \psi \frac{\partial \chi^*}{\partial z}) d\mathbf{S} \quad (2.11)$$

denotes the effect of the overlap of the two wave functions, where χ and ψ are the wave functions of the electron at the tip and the sample, respectively. The dependence of the tunneling current on the distance is also included in M . The exponential relation relating the work function can be obtained by applying the WKB approximation under the weak correlation condition, i.e.:

$$|M|^2 \sim \exp(-\sqrt{8m\phi z}/\hbar) \quad (2.12)$$

where ϕ is related to the work function of the tip and sample.

It is now necessary to make a few approximations to the expression for the tunneling current for further simplification. For low-temperature experiments, the $k_B T$ is generally relatively small, so the Fermi distribution function for very small thermal width can be approximated as a step function. The subtraction of the two step functions in the equation can form a gate function equal to 1 only between 0 and eV and 0 in the other intervals, so that the infinite integral can be reduced to an integral over a finite energy range.

Assuming that the tunneling matrix M is approximately constant over the energy range covered by the experiment, it can be expressed as a constant outside the energy integral, and the current expression can be simplified to the convoluted form of the density of states of the sample and tip as follows:

$$I = \frac{4\pi e^2}{\hbar} \exp\left(-\frac{\sqrt{8m\phi}}{\hbar} z\right) \int_0^{eV} \rho_s(E_F - eV + \epsilon) \rho_t(E_F + \epsilon) d\epsilon \quad (2.13)$$

The assumption of treating M as a constant is based on the assumption that the vacuum potential barrier between the tip and sample is relatively homogeneous and that the correlation between the wave functions of the tip and the sample is weak, i.e. there is no hybridization of the electron orbitals of the tip and the sample.

In practice, the tunneling matrix element is significantly affected by the arrangement of the atoms at the tip or the surface state of the sample, especially for a multi-band systems, where the tunneling spectra obtained in different cases may vary relatively widely and where careful discrimination is required and where the steady state at the tip is critical for STM measurements.

In most cases, we are more concerned about the information of the density of states of the sample, so the tip of the metal material with a flatter density of states near the Fermi surface is generally selected, thus the density of states of tip in the above equation can be placed outside the integral as an approximate constant term. The tunneling current is therefore proportional to the integral of the density of states of the sample, and differentiating the current with respect to the bias voltage V , we obtain:

$$\frac{dI}{dV} \propto \rho_s(E) \quad (2.14)$$

From this equation we can see that, under certain approximate conditions, the first order derivative of the tunneling current is proportional to the local density of states at the location where the sample tunneling occurs, which is the principle of the STM measurement of the local density of states of the sample.

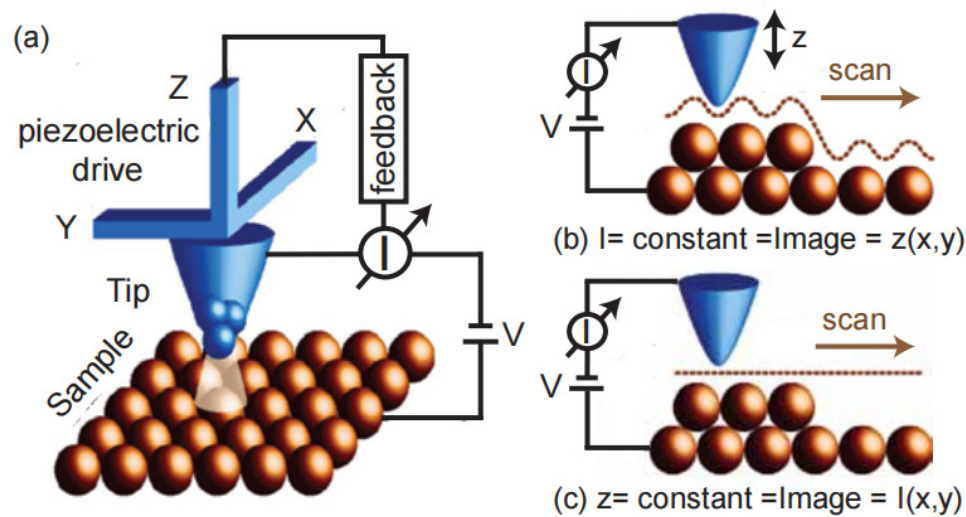


Figure 2.2: Schematic view of the working principle of an STM with the key operational modes. (a) A combination of the tip and the sample for the tunneling based imaging. (b) Constant-current STM mode. (c) Constant-height STM mode [25].

Figure 2.2 shows the two modes of operation often used in STM measurements, the constant-current STM mode and the constant-height STM mode.

In constant-current mode, the tunneling current is kept constant during the STM image scan and a feedback circuit is used to control the movement of the scanner in the z -direction, so that the distance between the sample and the tip is constantly changing. The constant-current mode is mainly used to observe samples with large surface variations, and is one of the common modes of operation for STM. The disadvantage is that some grooves between the particles on the sample surface cannot be accurately detected, and that the tip could be easily damaged when there are defects on the sample surface.

In constant-height mode, the height of the tip is kept constant during STM image scan and information on the surface variation of the sample can be obtained by changing the tunneling current. The constant-height mode can only be used for samples with small surface variations. The advantage is that the scanning speed is fast and the effect of noise and thermal drift on the signal can be reduced. In our measurement, the constant-current mode is used [26].

2.2 Principles of Raman scattering

Raman scattering is a two-photon process. A first photon with energy ω_i and momentum k_i is absorbed by the sample and a second photon with energy ω_s and momentum k_s is scattered off [27]. Through the principle of conservation of energy and momentum, the following can be surmised:

$$\hbar\Omega = \hbar\omega_i - \hbar\omega_s \quad (2.15)$$

$$\hbar q = \hbar k_i - \hbar k_s \quad (2.16)$$

where in the energy $\hbar\Omega$ and the momentum $\hbar q$ are transferred into the system. In inelastic scattering, the process starts with that of an excitation from the initial state $|I\rangle$ to a virtual state $|\nu\rangle$ before relaxation to a final state $|F\rangle$ occurs. In order to characterize this process a comparison between the energy levels of the initial and final states is necessary. Shown in Fig. 2.3 (a) is a process with a relatively low final state $|F\rangle$ energy level, called an anti-Stokes process, wherein the scattered photons exhibit a blue shift. In the event the final state $|F\rangle$ is located in a higher energy level, this is known as a Stokes process in which the scattered photons demonstrate a red shift. An illustration of such a process is given in Fig. 2.3 (b).

In the Raman process, high energies and small momenta are transferred to the system due to the dispersion characteristics of light, and the momentum of the probed excitation is close to zero (i.e., $q \approx 0$). A sketch of a Raman spectrum is displayed in Fig. 2.4, where the number of scattered photons $I_s(\Omega)$ is plotted as a function of the Raman shift Ω denoted in the units of wavenumber (cm^{-1}).

The peak positioned at $\Omega = 0$ originates from the elastically scattered photons. The inelastic processes are shown on either side of the incident energy and labeled Ω_1 and Ω_2 . The anti-Stokes peaks ($\Omega < 0$) have the same energy but are lower in intensity in comparison to the Stokes peaks ($\Omega > 0$). The relation between the Stokes and the anti-Stokes spectra is given by the principle of detailed balance which has the following form:

$$\frac{I_{AS}}{I_{ST}} = \left(\frac{\omega_i + \Omega}{\omega_i - \Omega} \right) \exp \left(-\frac{\hbar\Omega}{k_B T} \right) \quad (2.17)$$

where I_{AS} and I_{ST} are the rates of photons in the anti-Stokes and the Stokes processes, respectively. k_B is the Boltzmann constant and T is the temperature [26].

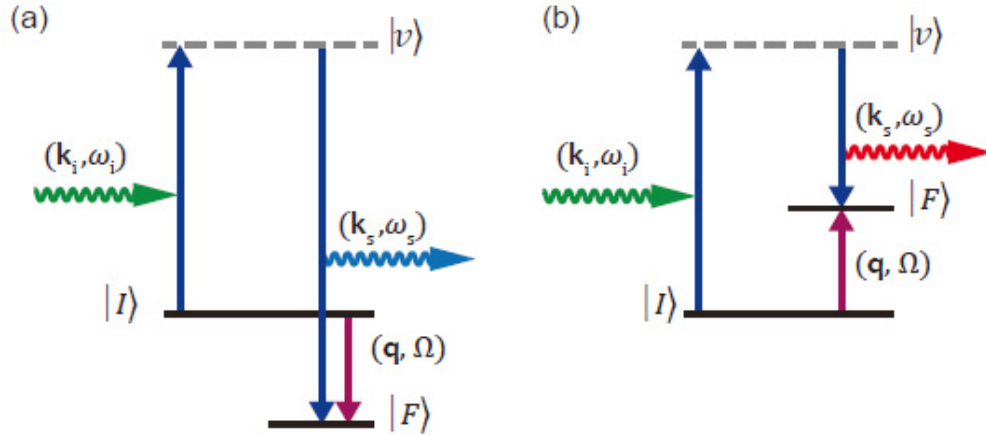


Figure 2.3: (a) anti-Stokes process with annihilation of an excitations which results in a blue shift for scattered photons. (b) Stokes process where an excitation is created and this results in a red shift for scattered photons [28].

Photons are not only characterised by their momentum and energy (k, ω), but also by their polarisation. One of the most powerful assets of Raman scattering is the selection rules. The excitations that are projected out when taking measurements can be selected by their symmetry.

The symmetry of the excitation Γ_x is that of the operator, that projects the initial state $|i\rangle$ with symmetry Γ_i onto the final state $|f\rangle$ with symmetry Γ_s . Therefore, the following can be deduced:

$$\Gamma_x = \Gamma_s \times \Gamma_i \quad (2.18)$$

where Γ_i and Γ_s are hereby represented by the polarisation vectors e_i and e_s [29]. All scattering processes that do not fulfill the condition specified in equation 2.18 are thus forbidden. The Raman scattering from phonons needs to obey this same condition, and for each phonon, a symmetry-dependent Raman tensor α can be assigned. More details about Raman selection rules can be found in chapter 4

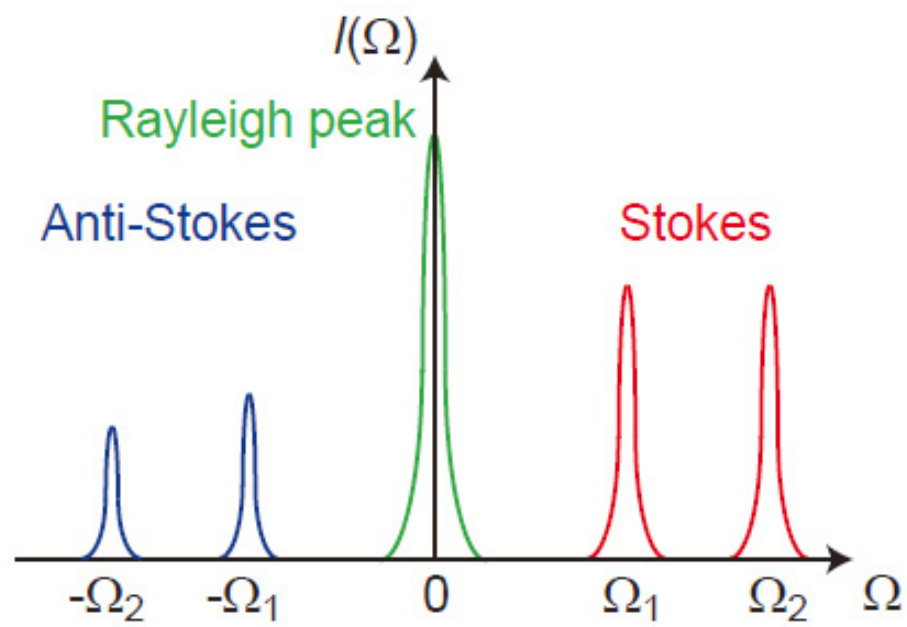


Figure 2.4: A Raman spectrum with different excitations. The Raman intensity $I(\Omega)$ is plotted as a function of the Raman shift (Ω)[26].

3 Setup

This chapter describes the experimental equipment, including the STM Setup, the Raman spectroscopy and the fabrication of the tips.

3.1 Scanning tunneling microscopy



Figure 3.1: Overview of the lab. The cryogen level monitor, temperature controller and SPM controller are shown housed on the left rack while the optical table with the cryostat and the optical components for Raman spectroscopy are on the right [26].

The overall layout of the lab can be seen in Fig.3.1. The sample holder was placed in a cryogenically pumped UHV cryostat together with the scanning tunneling microscope. This cryostat could be pumped to a pressure of 10^{-8} mbar and the minimum temperature that the system could attain was

20 K. As STM experiments are very sensitive to vibrations, four vibration isolators (Newport, S-2000 stabilizer) were utilized underneath the optical table. The instruments on top of the table were dampened by these vibration isolators to reduce mechanical vibrations. This system was equipped with the aforementioned cryogenically pumped UHV cryostat (Janis Research, CNDT series) to facilitate low temperature measurements [30]. During the experiment, the cryostat was flushed with nitrogen to remove any moisture and dust. The basic pressure that could be achieved before filling with LHe is 10^{-5} mbar and when UHV conditions were required, the system was baked out .

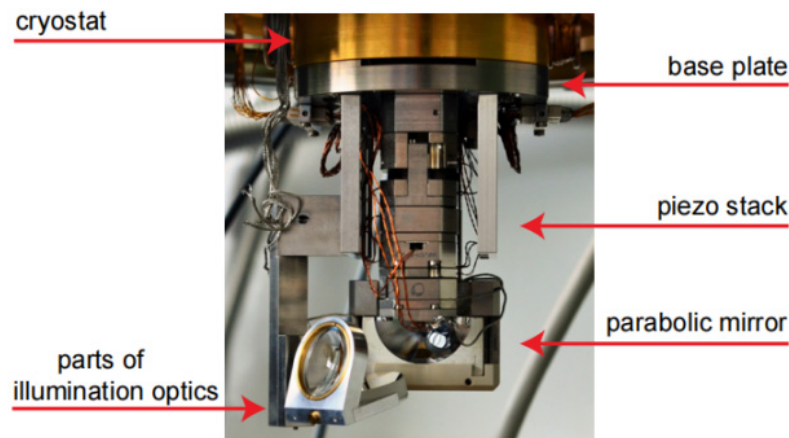


Figure 3.2: Microscope in the open cryostat. The piezo stack was located in the middle, with the parabolic mirror below the piezo stage for the Raman measurement [26].

Fig.3.2 shows a picture of the microscope unit and the internal optical components in the open cryostat. The microscope unit was mounted on a base plate and fixed to the cryostat in an upside-down position and part of the Koehler illumination optics system is shown in the lower left corner of the picture.

Fig.3.3 presents the inverted view of the disassembled microscope head. Importantly, when the tip needed to be replaced, the L-shape tip-holder was taken out and the new tip was soldered to the edge of the tip-holder by using indium. Also, the edges of the sample were glued with conductive silver paste, and as soon as the sample was attached to the sample-holder, the electrical conductivity of the sample was monitored with a multimeter to ensure that the tunneling current could pass through before the whole assembly was mounted on the microscope head.

The bottom of the cryostat was attached to a base plate fitted with a height adjustable device. This plate can be moved up and down in a controlled way with an accuracy of approximately $10 \mu\text{m}$ to

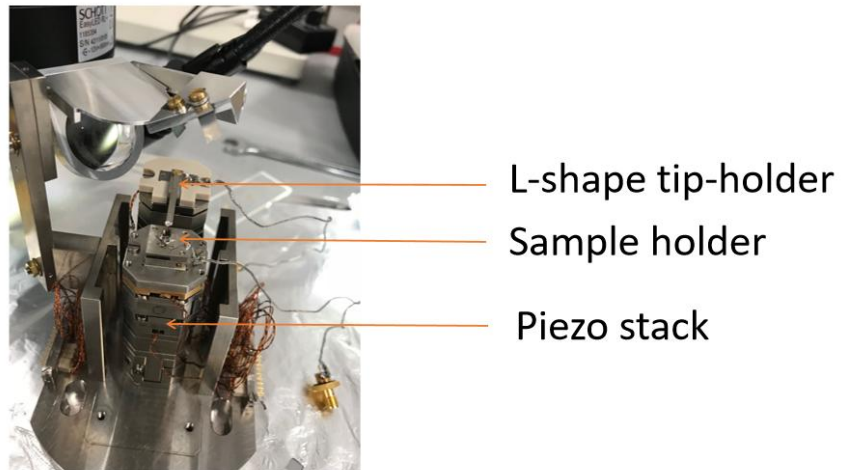


Figure 3.3: Inverted view of the disassembled microscope head. The L-shaped tip-holder was placed upside down at the bottom of the unit and the sample-holder affixed directly above it. Of note, the L-shaped tip-holder had to be removed when it required replacement.

compensate for the thermal contraction of the components inside the cryostat while cooling.

In order to avoid collisions between the tip and the sample, the operation was not carried out in a constant height mode, but in a constant current mode with variable height. All control units were assembled in a cabinet next to the cryostat, and the measurements were taken and processed using the program “Daisy”.

Fig.3.4 gives an overview of the user interface of the “Daisy” program. It was developed by Attocube System AG specifically for this type of measurement. As noted, the parameter panel is displayed on the left side of the interface where the necessary parameters can be input and changed (such as the scanning range, scanning speed, PID values, etc.). An open feedback loop ensures that the current is kept constant. When the STM starts operating, the constant current mode is selected and the scanning area changes its z-position as the piezoelectric element passes through different positions due to the height variation. The z-position is again recorded digitally based on the current of the piezo element. Therefore, the topological information of the sample surface can be depicted.

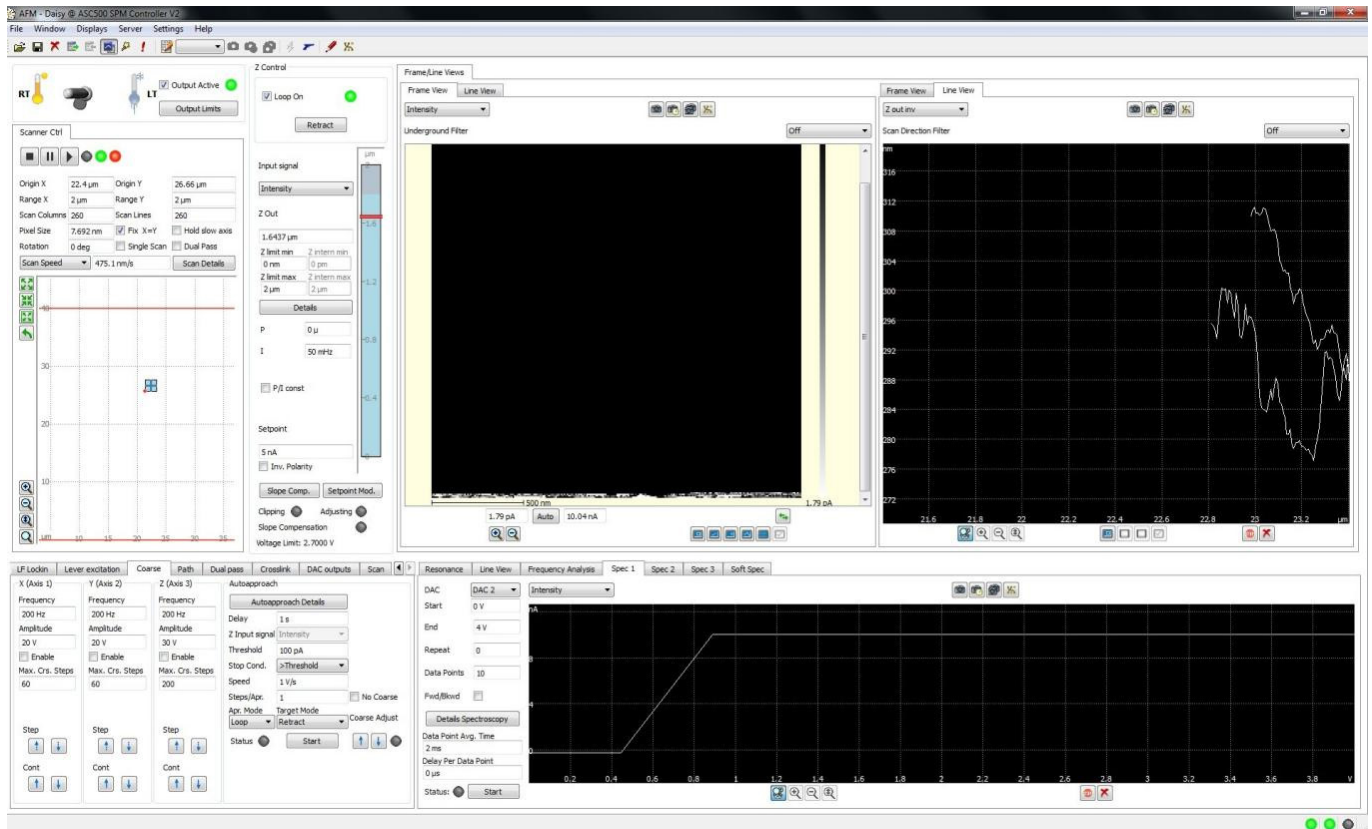


Figure 3.4: Screenshot of the user interface of the program “Daisy”. The parameter panel is displayed on the left side, the first image on the right shows the topological image of the sample, and the second image is the scan line of the scanning area, showing the change in height over the line being scanned.

3.2 Raman spectroscopy

3.2.1 Optical path

The diagram of the optical path of the Raman measurement is shown in Fig.3.5. Within it, the monochromatic light with a wavelength of 532 nm is emitted by a diode-pumped solid state (DPSS) Laser (Coherent Sapphire SF). The laser passes a lens with the focus length of $f_{L1} = 10\text{mm}$ first, then a pin hole was mounted to obstruct the stray light past the lens as the focus of the lens overlaps with the position of the pinhole. Another focus lens with the focus length of $f_{L2} = 60\text{mm}$ is used to generate a light beam with a diameter of 6mm. After that, the laser beam is reflected by a mirror set at an angle of 45° .

The laser beam then passes through a $\lambda/2$ plate, the purpose of which is to adjust the laser power. After

the half-wave plate, a polarizer is present for setting the polarization of the incident light after which an optical plate is used for focusing procedures. The optical flat is made of quartz and has a silver coating on one side. The laser light is reflected by the silver coating layer by around 95%-98% of its initial intensity, but only 4% of the intensity can be reflected by quartz surface. Therefore, a main beam in the middle and two other dark beams can be formed. The optical flat divides the laser beam into three strictly parallel beams.

The laser beam then passes through a beam splitter and enters the vacuum chamber. A parabolic mirror was mounted on the scanner to focus the laser on the surface of the sample. The laser light interacts with the sample surface and from this, Raman scattered light is emitted, which is then collected by the parabolic mirror and reflected back towards the beam splitter. This light is further reflected by the beam splitter and collected by the focus lens. The laser beam then passes through a filter in order to further reduce the stray light. Subsequently, another polarizer, acting as an analyzer, is used to select the desired polarization of the scattering light combined with another $\lambda/2$ plate, which has the same function as the first $\lambda/2$ plate. Finally, the light passes through the focus lens and enters the spectrometer.

3.2.2 Focusing and alignment procedure

Before starting Raman measurements, the optical path was aligned and optimized, beginning with the shape of the laser spot which was configured as a regular circle. The laser beam was then adjusted with a target to confirm that the laser beam passed through the center of each optical element. Next, to confirm that the light passed through the center of the entrance to the spectrometer, the optics in front of the spectrometer were checked. If the light did not track as intended, the position of the optical plates, polarizing mirrors, half-wave plates, focusing mirrors were adjusted accordingly. Finally, the main beam in the middle was blocked to allow the other two lateral beams to pass through. Fig 3.6 presents the varying output of the focusing procedure using the optical flat. During the alignment, two parameters could be changed: the z-height of the sample-holder; and the angle of the optical flat. The sample was illuminated by a Koehler illumination system and the two lateral laser spots can be seen on the screen. In the Koehler illumination, the image of the light source is defocused in the sample plane, thus the illumination source is not visible in the image. The visible output from different alignment configurations are shown in Fig.3.6.

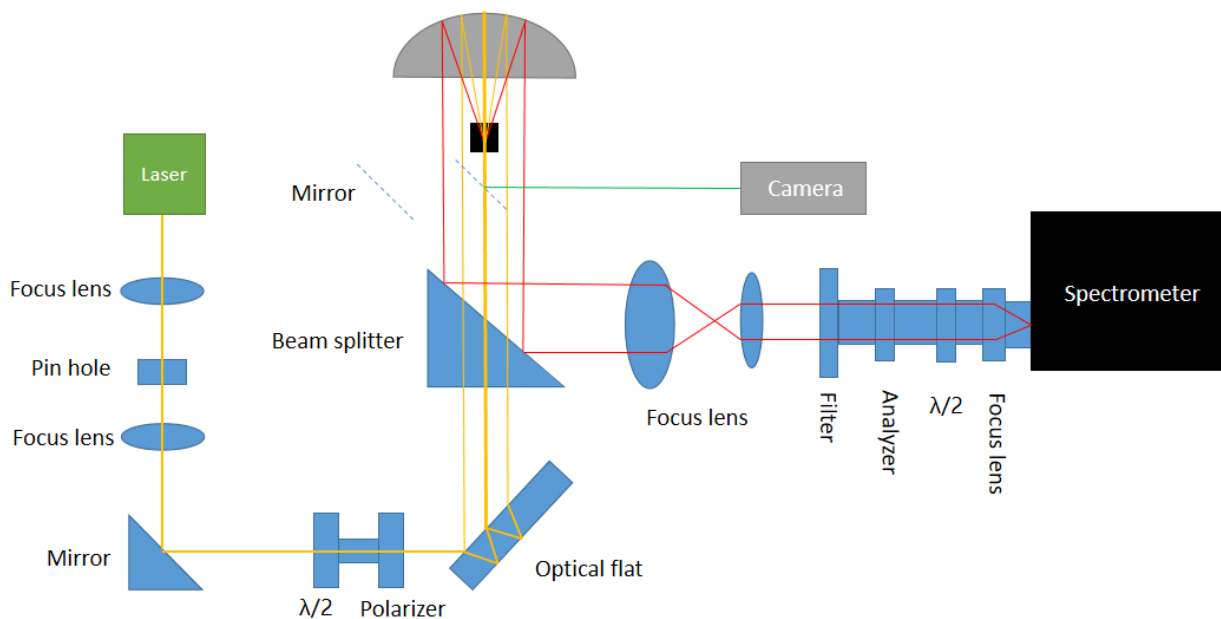


Figure 3.5: Diagram of the optical path of Raman measurement. A solid-state Laser produces a beam of monochromatic light with wavelength of 532 nm. The light passes through two lenses either side of a pin hole, the latter of which fixes the beam diameter. A mirror reflects it through a half-wave plate and a polarizer, the resulting beam is then aligned and split into three beams by an optical flat. A beam splitter and parabolic mirror contribute to focus the laser onto the surface of the sample. The beam splitter further reflects the beam through a final focus lens that collects the incident light. A final array further decreases the stray light which then enters the spectrometer.

The optical elements which collect the scattered light also have to be aligned. For this purpose, a 30° tilted silicon sample is used. The advantage of using a tilted sample is that the direct reflex is reflected again on the parabolic mirror and exits the cryostat parallel to the incoming laser beam. This direct reflex is used as a reference to align the collection optics. For our measurements, the alignment was done for an incoming laser beam which was reflected at the center of the parabola [31].

3.2.3 Measurement with Raman spectroscopy

The Raman measurement can be controlled via the computer program “*Light field*”. Fig.3.7 illustrates its user interface and the parameter panel is shown on the left. The measurement process entails, first, loading the experimental parameters for measurement, then new background data (without exposure)

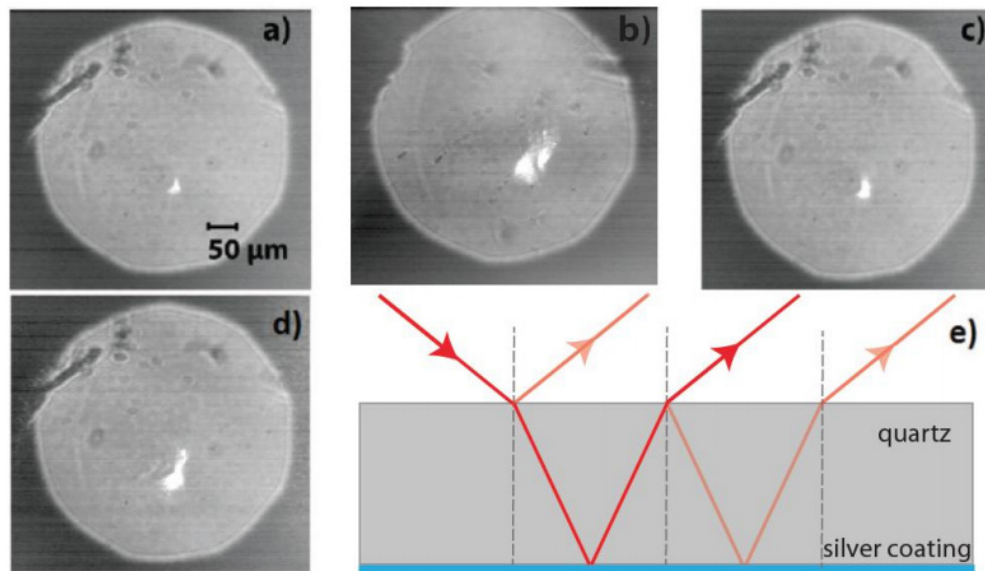


Figure 3.6: Focusing with the optical flat. Both the sample's z-position and the angle of the optical flat were iteratively adjusted to make the two lateral beams coincide: (a) unfocused since only one spot can be seen; (b) two spots are visible but they do not overlap; (c) focused conditions, that the two spots overlap and the focus is on the sample; (d) the spot generated by the central beam is visible and overlaps with the other two spots; and (e) illustration of the optical path in and out of the optical flat. The central strong light is depicted as the red line and the weaker lateral light is shown in the orange lines [30].

is acquired, whereupon the reference CCD image is checked to confirm the measurement wavelength region (which is supposed to include the elastic and inelastic scattering parts). Finally, the measurement program is run to obtain the refined Raman spectrum.

3.3 Tip fabrication

Knowledge of the atomic structure of scanning tunneling microscope (STM) probes is essential for improving spatial resolution and for the reliable interpretation of experimental data. Shortly after the invention of STM, it was discovered that only probes with a single atom at the point of a sharp tip could provide stable and reliable imaging with atomic level resolution. Although several forms of monatomic

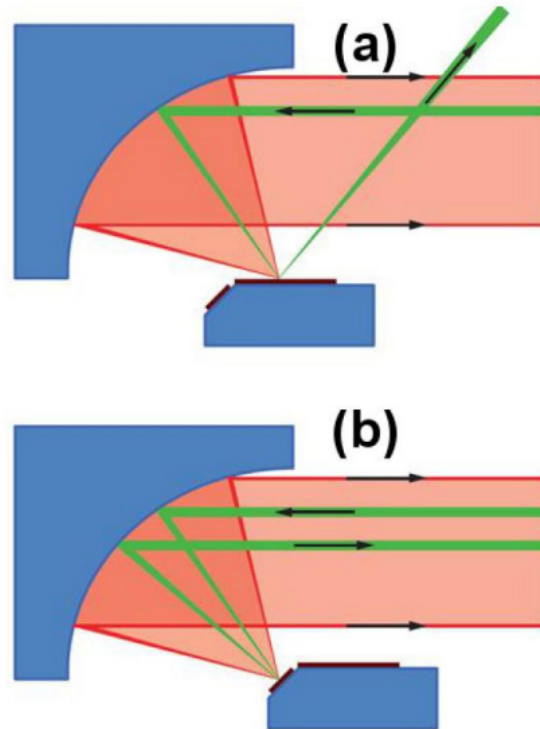


Figure 3.7: Schematic drawing of the laser beam reflection on a silicon sample. (a) The silicon sample is not tilted. The direct reflex is not emitted in the direction of the parabolic mirror. (b) The silicon sample is tilted. Therefore, the direct reflex is reflected again on the parabolic mirror and exits the cryostat parallel to the incoming laser beam [31].

terminated tips can facilitate atomic resolutions, such resolutions can only be achieved if the sharp tip collects the vast majority of the tunneling current through the electron orbitals of the single front-most atom closest to the sample surface [32].

In order to obtain a sharper gold tip, the etching of the gold tip was optimized by Nitin Chelwani and Gabriele Rager. Fig.3.9 (a) shows the tip etching setup. For the etching of gold, 37% fuming hydrochloric acid (HCl) was recommended as the electrolyte [20]. For this work, the diameter of the gold wire used was 100 μm and that of the platinum ring was 250 μm . Once the etching reaction was initiated by means of the manual switch (S), the platinum ring directed the current flow around the gold wire, with periodic pulses as stated above. When the contact between the tip and the solution broke, the etching was automatically stopped, leaving a sharp tip with the desired shape and with varying degrees of sharpness [30].

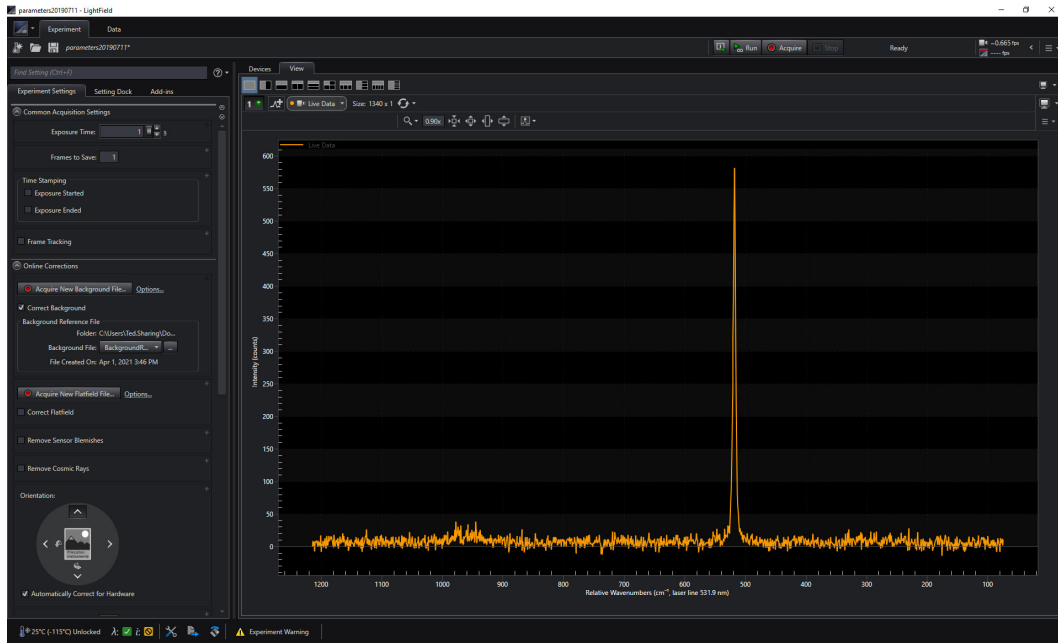


Figure 3.8: The interface of the program *Lightfield*. The Raman spectrum of Si(110) sample is shown in the picture.

The etched tip was characterized in two steps. First, the tip was analyzed using an optical microscope, which provided information about its geometry. Tips that possessed a shape that was considered suitable for experimental use were placed under the SEM for further observation. During the tip fabrication process, the gold wire was annealed at 800 °C for 6 hours. A SEM image of the tips is shown in Fig. 3.10.

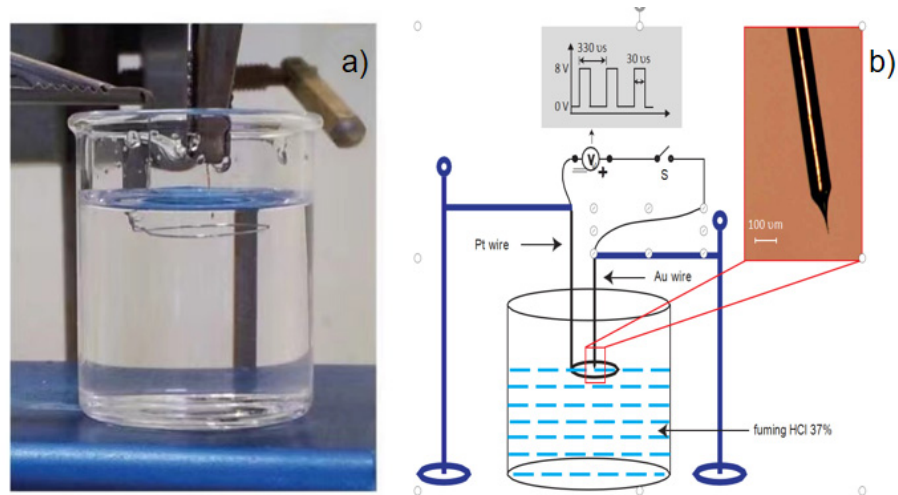


Figure 3.9: (a) Tip etching setup. The tip is held in a crocodile clip and immersed in the etching solution, (b) the sketch of the electrochemical tip-etching setup, the voltage pulses are 30 μs in duration and they are separated by 300 μs [26].

Annealed gold wire at 800°C & 6h

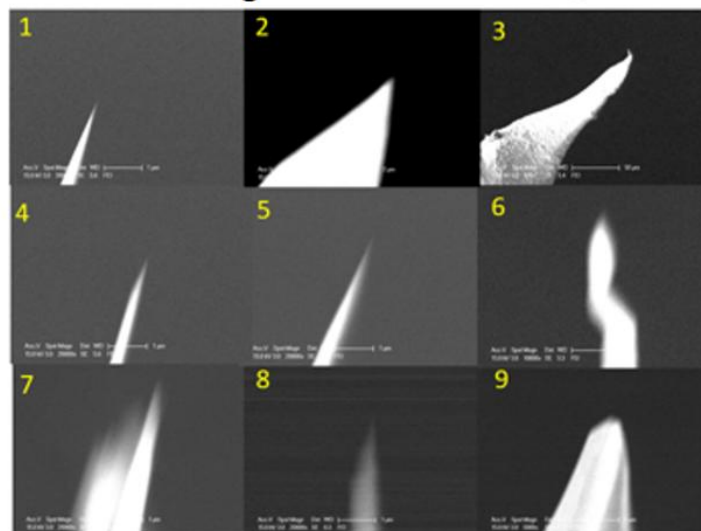


Figure 3.10: The SEM images of tips. The gold wire was annealed at 800 °C for 6 hours.

4 Measurement

This chapter describes the measurements of Au and 1T-TaSe₂ samples in STM and the spectra of Si and 1T-TaSe₂ samples under Raman spectroscopy.

4.1 STM experiment

4.1.1 Noise spectrum

Before taking any STM measurements, the background noise of the system was measured first. Fig.4.1 shows the time-dependent current and the background noise spectrum without tip approaching.

The noise spectrum was assembled by the software's built-in Fourier analysis function. In the current spectrum, the x- & y-axes represent the time and the real-time current intensity, respectively, while in the background noise spectrum, the frequency is represented in x-axis instead.

Noise is an important matter in STM systems, given that low noise is often critical to STM measurements [33]. Generally, it comes in two forms: mechanical; and electrical noise [20]. Mechanical noise is caused by vibration, such as that of buildings, waves, pumps in operation, fans in connected apparatus, and from the cryostat filled with low temperature liquid. Electrical noise comes mainly from coupling with the electrical supply, thus its frequency is an integer multiple of 50 Hz which is the frequency of the power outlet.

In light of this, before the STM measurement, some procedures were undertaken to lower the noise levels. For the electrical noise, the grounded wire and BNC cable between the feed-through and pre-amplifier were moved away from the system while some small mechanical noises at low frequency were also diminished by lifting the optical table on top of vibration isolators.

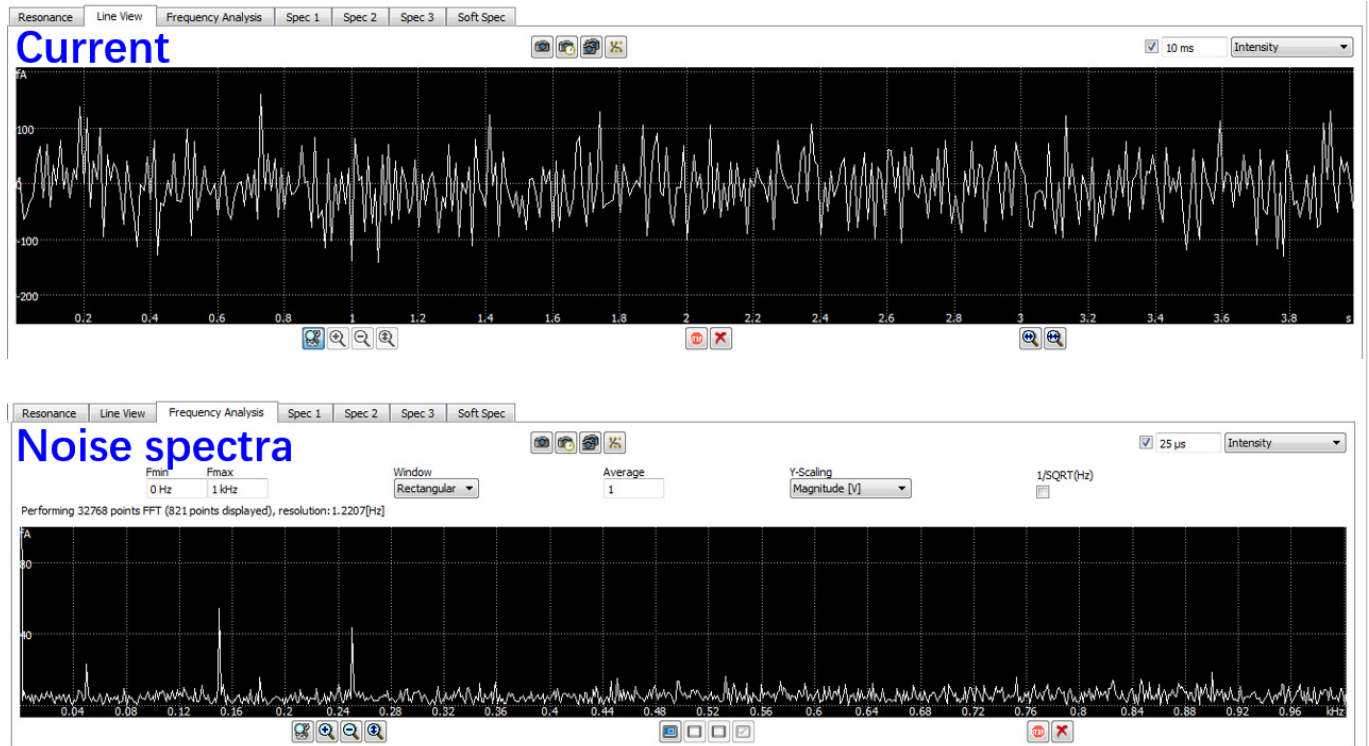


Figure 4.1: Current and noise spectra without tip approached. The current intensity is less than 100 fA. The peaks of the noise spectrum are located at 50 Hz, 150 Hz and 250 Hz. All noise intensities are less than 80 fA/sqrt(Hz).

4.1.2 Parameters setting of the Attocube software

Concerning the STM measurements, there are several key parameters for running STM software, i.e., the calibration parameters and polarity parameter of the piezo, P/I, threshold current, tunneling current, bias voltage, scan range and scan speed. During the measurement, the parameters were set as shown in Tab. 4.1.

4.1.3 STM measurement on amorphous gold

The first measurements on this setup were made on amorphous gold, with the aim of demonstrating that the instrumentation was in proper working condition. Before inserting the sample into the piezo head, the gold sample was annealed at a temperature of 800 °C for 6 hours in order to remove the contaminants. Due to the higher stability of gold compared to other materials, it was easier to tune the parameters of the system during the scanning of gold samples, and to obtain more accurate noise

Table 4.1: Parameter setting of the attocube software

Parameters	Auto approach	Scanning
x-axis		6 V & 40 μm
calibration		300K
y-axis		6 V & 40 μm
calibration		300K
z-axis		3 V & 2 μm
calibration		300K
polarity	backward	backward
P	$\sim 1 \mu\text{A}$	$\sim 1 \mu\text{A}$
I	20 Hz . This value determines the approach speed.	50 mHz
Threshold current	100 pA	/
tunneling current	500 pA . This value determines the approaching speed.	It depends on the noise. For a lager noise, we should set a lager value. Typically, it can be set from 100 pA to 5 nA .
bias voltage	2 V	500 mV
scan range	/	Less than 40 μm * 40 μm
scan speed	/	No limit. It is suggested to control the time in 30 min for one image.

information. Most importantly, it was more convenient to verify if the tip was qualified and stable during the scanning process of gold sample. As the tip could not be mounted easily in the system as used in this research, the measurement of gold was performed as a test measurement in order to select a tip that could work well.

After several sets of measurements were taken and with periodic replacement of the tip, a finalized gold tip was settled upon to be used in the main experiment. A relatively stable and clear image of the topography of amorphous gold sample was obtained.

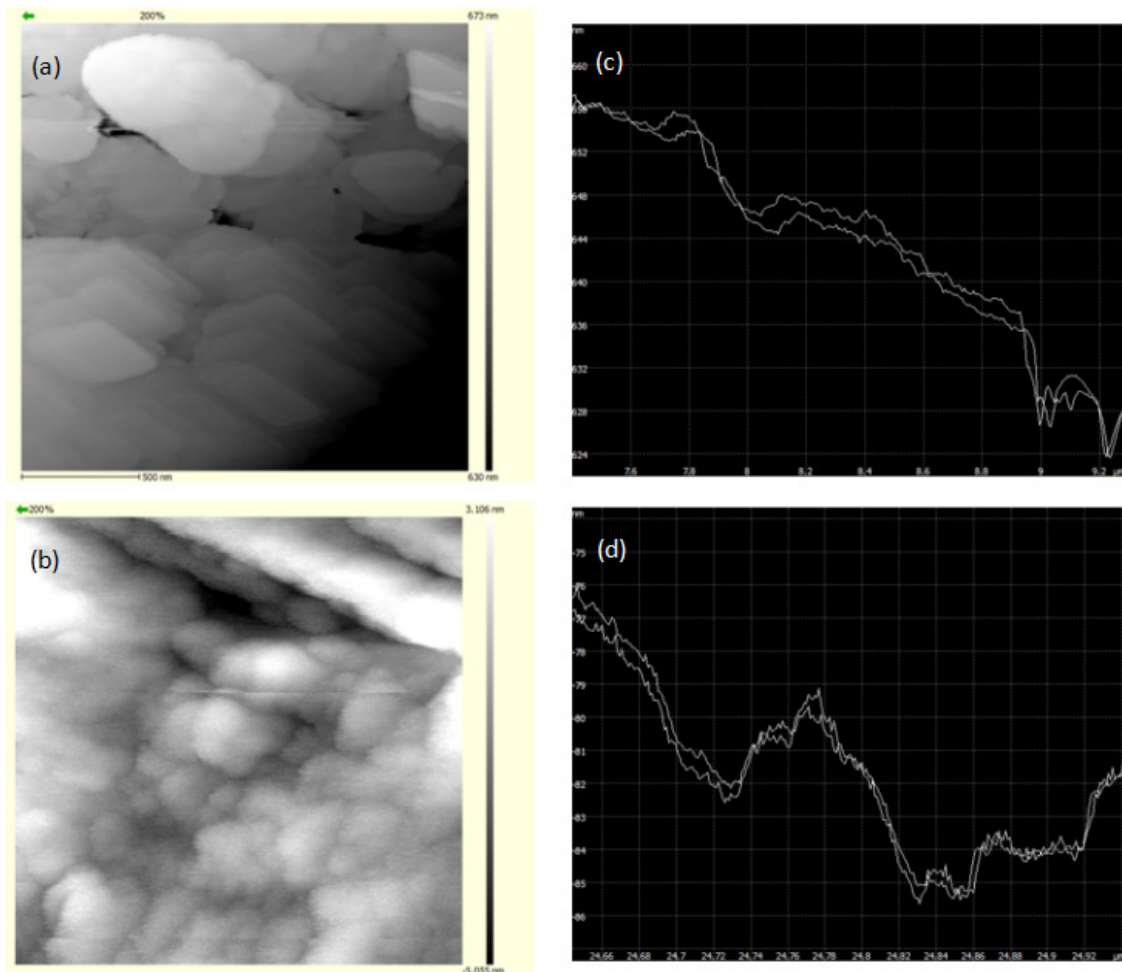


Figure 4.2: The topography of amorphous gold sample scanned by STM and the scanning lines. The scanning lines (abscissa: horizontal scan line, ordinate: topography) are shown in Fig.4.2(c) in the backward, and (d) forward scanning direction. These scan lines correspond to the middle lines in Fig.4.2(a) and (b), respectively.

Fig.4.2 shows the topography of two different amorphous Au samples. The grain boundaries of the gold are visible in this graph. The experiment was carried out in air temperature of 22 °C and a humidity

of less than 40%, in order to avoid interference with the tip performance due to excessive water vapor molecules. As the sample was not absolutely parallel to the movement of the piezo-scanner, a “slope compensation” function was active to correct for the tilt. During the scanning process, the p and I values of the PID feedback system were constantly adjusted in the piezo-scanner, as well as the scanning speed, in order to mitigate the effects of the environmental noise and to avoid the tip resonance. Since the main objective was to test the topography of 1T-TaSe₂, the system was not subjected to UHV conditions and filled with liquid Helium in the event that the tip did not meet our requirements and needed to be replaced.

4.1.4 STM measurement on Au(111)

Although the topographical image of the amorphous gold sample was obtained, the spatial resolution of the system in the z-direction was not easily realized due to the large surface fluctuations. Therefore, the single crystal gold Au(111), which has a flatter surface structure, was used for the next experiment to observe the z-directional resolution of the system. The Au(111) sample was cleaned with the same annealing process as the amorphous gold prior to measurement.

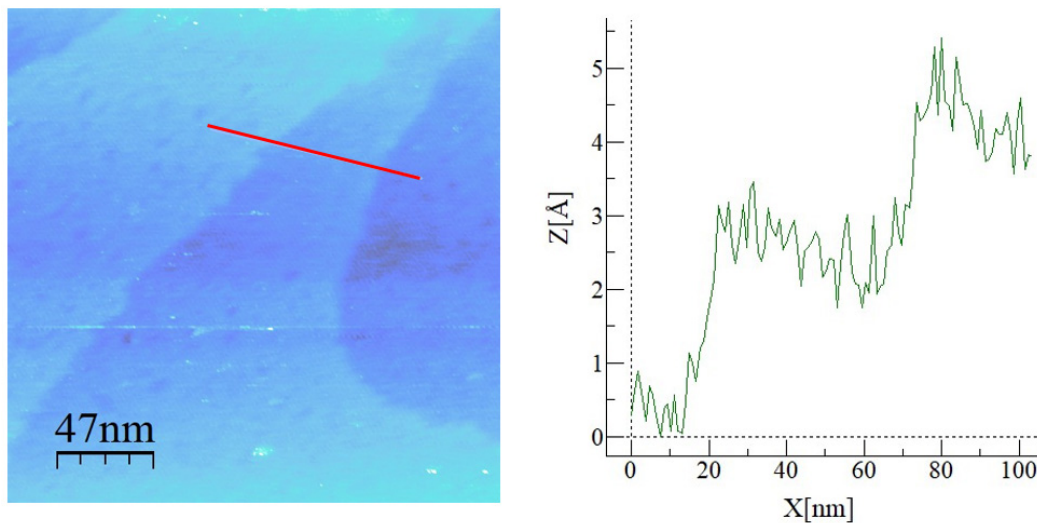


Figure 4.3: (a) The measurement of the topography of Au (111) scanned by STM. (b) The distribution of the atomic layer heights in the area corresponding to the red line in Fig.4.3(a). The x-axis denotes the distance from each point on the red line to the left end of it, y-axis denotes the relative height of the atomic layers at each point on the line.

The topography of Au(111) is shown in Fig.4.3 (a), from which the atomic steps can be clearly resolved.

The boundaries between two atomic layers on the surface are located between the light and dark blue areas, and each step corresponds to a single atomic layer of gold atoms. The height of the atomic steps in the region indicated by the red line is shown in Fig.4.3(b), which is approximately equal to 220 pm. This result infers that the Attocube scanner has a z-axis resolution superior to 220 pm.

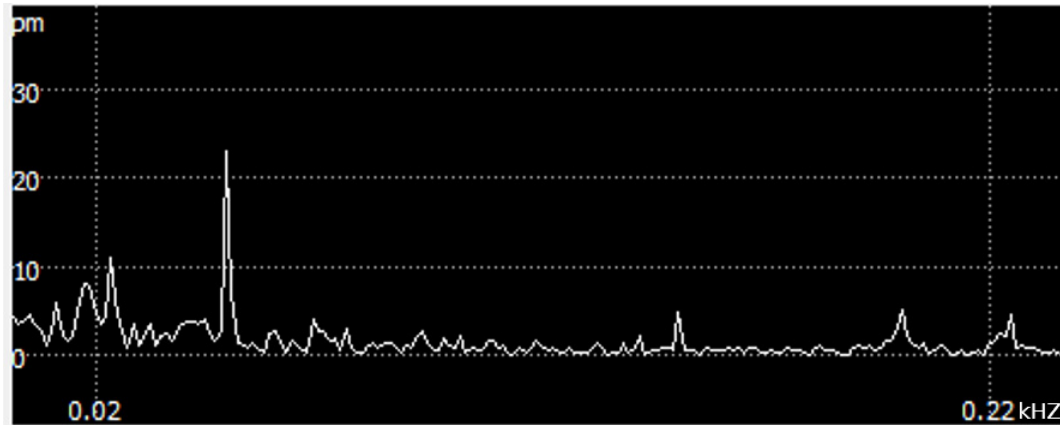


Figure 4.4: The FFT spectrum of time-dependent z. The peak of the spectrum is located around 50 Hz.

With the time-dependent FFT of z, the resolution of the z-axis can be directly obtained as shown in Fig 4.4. The highest peak is around 22 pm. It means that the limit of the resolution is 22 pm.

4.1.5 STM measurement on 1T-TaSe₂

After the test measurements of the gold samples, the system was maintained in its original conditions and the 1T-TaSe₂ sample was placed on the sample-holder. For removing contaminants and obtaining a flat surface, the sample was cleaved with adhesive tape. Then, the Dewar was filled with liquid nitrogen to cool the system down to around -160 °C and reach a pressure of approx. 10^{-6} mbar.

Even many attempts and adjustments, a clear topographical image of 1T-TaSe₂ was not obtained. Fig. 4.5 shows the topography sample surface scanned by STM. The surface characteristics of 1T-TaSe₂ cannot be observed from this picture, nor is the expected CDW phenomenon discernible.

The reason for this was surmised to be the contamination of the sample after being cleaved. Due to the limitations of the instrument design, an in-situ cleavage of the sample was not possible in this experiment, which resulted in the tip also adsorbing impurities. Therefore the tunneling current could be unstable.

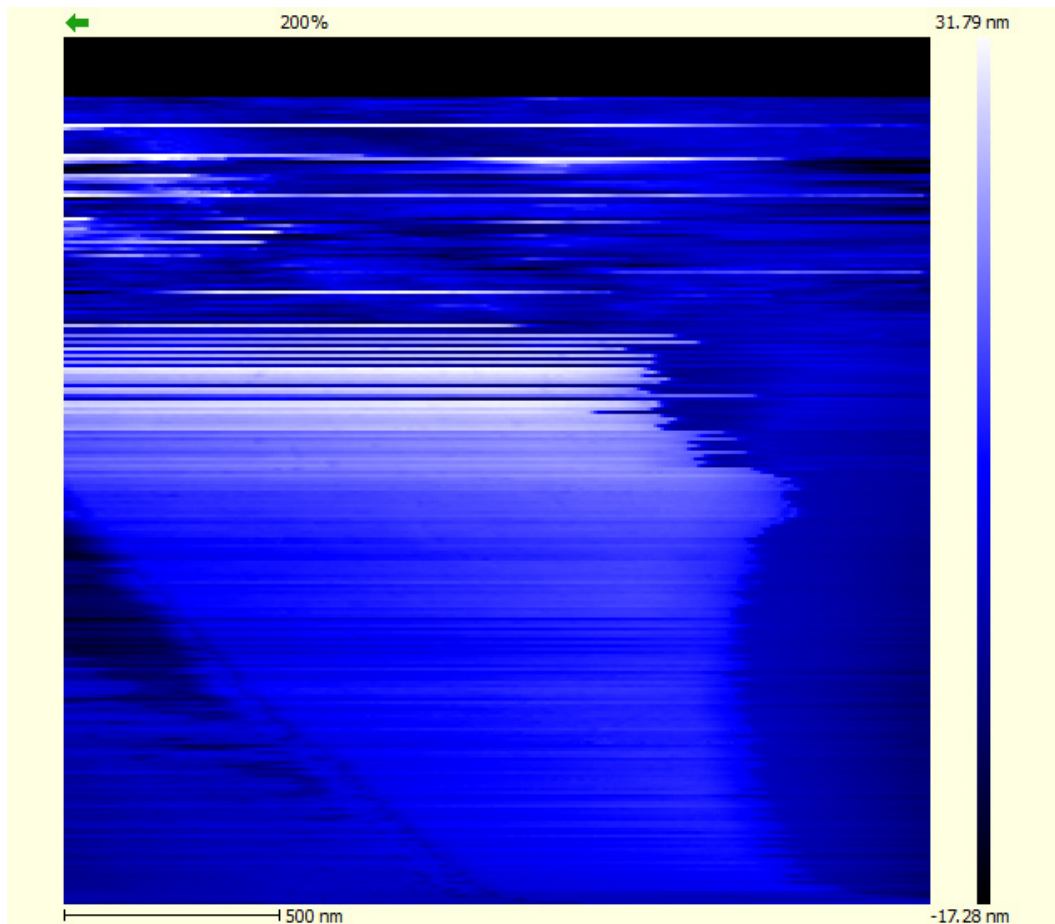


Figure 4.5: The topography of the 1T-TaSe₂ surface scanned, the abscissa and ordinate are the axes of the TaSe₂ surface and the blue scale denotes the topography.

4.2 Raman measurement

4.2.1 Raman spectra of Si(110)

Before the measurement of the Raman spectrum of 1T-TaSe₂, the spectrum of silicon was tested first for the purpose of improving the collimation of the optical path by adjusting the lenses and laser light during the measurement [34]. Silicon has a cubic diamond structure and for single-crystalline silicon, the Raman spectrum has a phonon peak at 520 cm⁻¹ obeying T_{2g} symmetry [35]. As this phonon is very pronounced and narrow, silicon is widely used for calibration purposes in Raman spectroscopy.

The Raman spectrum of Si is shown in Fig.4.6. The wavelength of laser light was 531.9 nm and the exposure time was set to 1 second, while the polarization direction is taken as XY direction, and

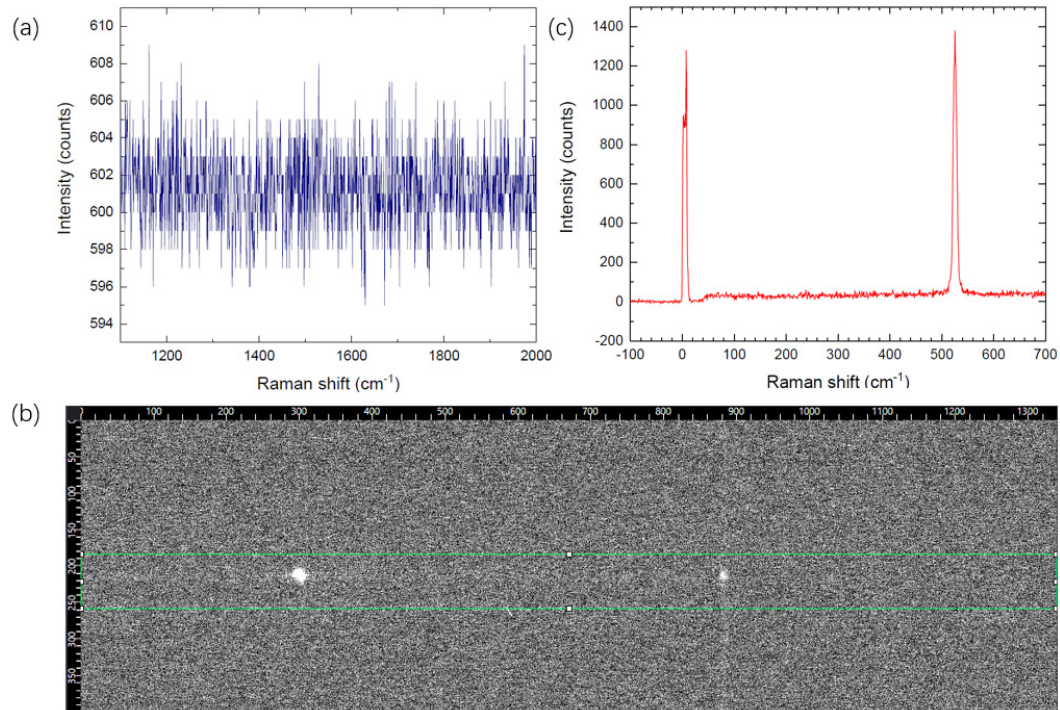


Figure 4.6: Raman measurement process. (a) Typical background data. (b) CCD image for Si sample, the brighter spot corresponds to light with the Raman shift of 519 cm^{-1} and the darker spot represents the light with the original wavelength of the laser. (c) Raman spectrum of Si (110) sample.

the measurement was carried out at room temperature. Fig.4.6 (a) shows the background data of the measurement. By adjusting the optical flat and other optical lenses, the highest degree of Raman intensity was finally reached. Fig.4.6 (c) shows the Raman spectrum of Si (110) sample, and the peak of the Raman spectrum appears around 519 cm^{-1} , which was as expected.

4.2.2 Raman measurement on 1T-TaSe₂

In this chapter, the Raman spectral results of 1T-TaSe₂ will be presented.

The experiments were initially conducted at low temperatures, for which liquid helium was filled into a Dewar. The chamber was pumped to a pressure of 2.2×10^{-8} mbar. Since there is a finite thermal resistance between the sample holder and the He bath, it was not possible to cool it to the temperature of the liquid helium, i.e., 4K. The experiment was started at a temperature of 20K and then the temperature

gradually increased, with measurements taken at increments of 5K, until it reached 295K.

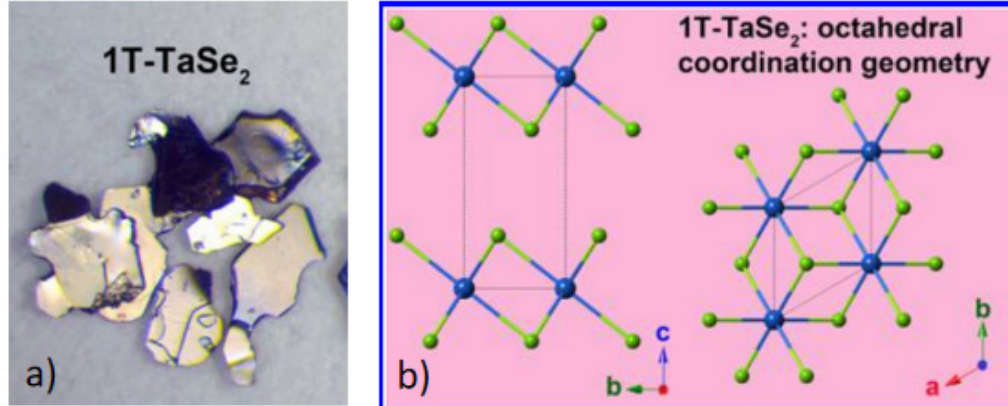


Figure 4.7: (a) The photo of 1T-TaSe₂ sample, (b) The crystal structure of 1T-TaSe₂. Blue circle represents the Ta atom and green circle represents Se atom, respectively [36].

The crystal structure of 1T-TaSe₂ is shown in Figure 4.7(b). 1T-TaSe₂ has a layered crystalline structure, consisting of planes of hexagonally arranged tantalum (Ta) atoms sandwiched by two selenium (Se) layers coordinating around the central Ta atom in an octahedral arrangement. The three atom thick Se-Ta-Se layers are weakly bound via a Van der Waals interaction along the direction of the c-axis [37, 38].

The space group of 1T-TaSe₂ is P63/mmc (No.194). According to the Raman selection rule, there are 7 Raman activated modes, i.e. 2A_{1g}, 2E_{1g}, 3E_{2g} [35]. Their Raman tensors can be written as follows,

$$\begin{aligned}
 A_{1g} &= \begin{bmatrix} a & 0 & 0 \\ 0 & a & 0 \\ 0 & 0 & b \end{bmatrix}, E_{1g} = \begin{bmatrix} 0 & 0 & 0 \\ 0 & 0 & c \\ 0 & c & 0 \end{bmatrix}, E_{1g} = \begin{bmatrix} 0 & 0 & -c \\ 0 & 0 & 0 \\ -c & 0 & 0 \end{bmatrix}, \\
 E_{2g} &= \begin{bmatrix} d & 0 & 0 \\ 0 & -d & 0 \\ 0 & 0 & 0 \end{bmatrix}, E_{2g} = \begin{bmatrix} 0 & -d & 0 \\ -d & 0 & 0 \\ 0 & 0 & 0 \end{bmatrix},
 \end{aligned} \tag{4.1}$$

The coordinates of the samples relative to the experimental space are shown in Fig. 4.8. The a-axis of the sample is parallel to the x-axis of the apparatus. The Raman intensity can be expressed as below:

$$I \sim |e_s^* \alpha e_i|^2, \tag{4.2}$$

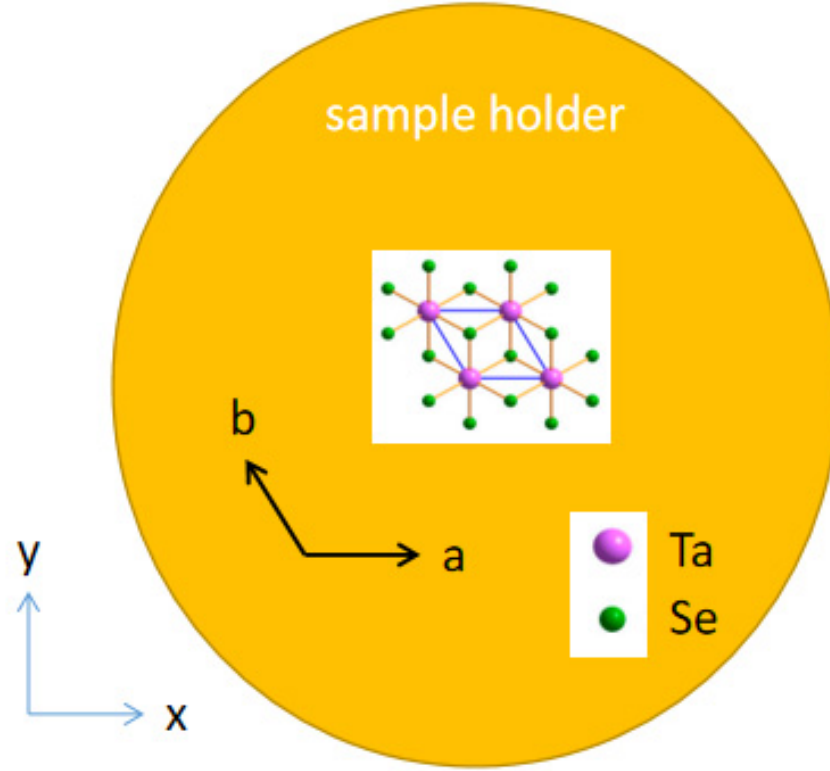


Figure 4.8: The coordinates of the samples with respect to the instrumentation layout.

where e_s is the polarization vector of scattering light, e_i is the polarization vector of incident light, α is the Raman tensor. To confirm whether a phonon mode can be observed in a certain symmetry channel, the Raman intensity should be calculated according to Eq. 4.2. For example, if we set the XX channel, the polarizations of both incident light and scattered light are parallel to the x-axis. Then, the Raman intensity of the XX channel for A_{1g} mode is read as:

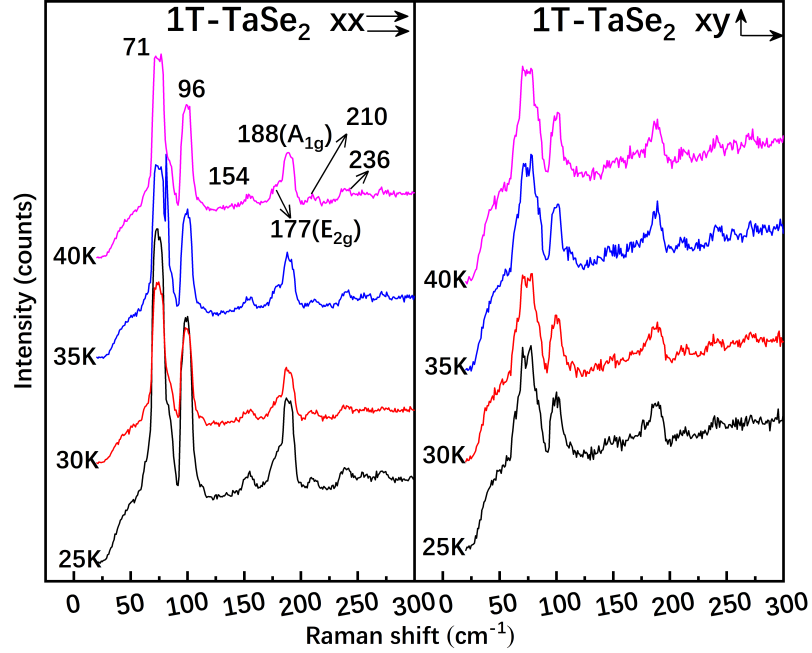
$$I^{XX} \sim |(1 \ 0 \ 0) \begin{bmatrix} a & 0 & 0 \\ 0 & a & 0 \\ 0 & 0 & b \end{bmatrix} * \begin{pmatrix} 1 \\ 0 \\ 0 \end{pmatrix}|^2 = a^2 \quad (4.3)$$

This means that the A_{1g} mode is observable in the XX channel. Based on this principle, XX and XY channels are listed in Tab. 2.

Figure 4.9 shows the comparison of the Raman spectra of 1T-TaSe₂ with different polarization directions of XX and XY in the temperature range of 25K to 40K as stated. In the absence of lattice distortion,

Table 4.2: Symmetry channels and the related Raman modes in 1T-TaSe₂

Symmetry channels	Polarization orientation	e_i^*	e_s^*	Raman modes
XY	$\uparrow\rightarrow$	(1 0 0)	(0 1 0)	E_{2g}
XX	\Rightarrow	(1 0 0)	(1 0 0)	$A_{1g} + E_{2g}$

Figure 4.9: The Raman spectra of 1T-TaSe₂ with different polarizations in the temperature range of 25K to 40K.

the Raman spectra of 1T-TaSe₂ in XX channel should consist of a pair of peaks with A_{1g} and E_{2g} symmetry. According to the literature, these peaks should occur between 150-250 cm^{-1} . We identify the Raman lines between 150-250 cm^{-1} as either arising from the normal Raman-active phonons of 1T-TaSe₂, or new Raman-active phonons due to the collapse of the optical-phonon dispersion curves in the presence of a commensurate superlattice [15]. In the studied temperature range, these peaks should shift in frequency with increasing temperature. The peak at $\sim 187 \text{ cm}^{-1}$ can be assigned as A_{1g} , while the peak at $\sim 177 \text{ cm}^{-1}$ is E_{2g} symmetry. The $\sim 154 \text{ cm}^{-1}$ Raman peak maybe originates from the zone-folded phonons in the C-CDW phase of 1T-TaSe₂ [36].

In addition, the other two Raman peaks are located near 210 cm^{-1} and 230 cm^{-1} , but there is uncertainty

concerning whether these belong to the E_{2g} or A_{1g} symmetry.

In the polarization direction of XY, the peak of A_{1g} 187 cm^{-1} should not occur, but is nonetheless observable. One possible reason is that when the sample was mounted, the a-axis of the sample was not strictly parallel to the x-axis of the system, therefore all the Raman components belonging to other polarization directions would appear. Another reason is potentially the parabolic mirror in the system which may have caused some rotation of the polarization. As the light reflected by the sample incidents at different angle with respect to the parabolic mirror and is re-reflected differently, the polarization of the scattered light was changed. Thus the collected scattered light has a contribution of different polarization. Furthermore, the aluminium coating of the parabolic mirror may cause a phase shift between the incident and reflected light, producing elliptical polarization light rather than linear polarization on the sample [26].

Figure 4.10 shows the Raman spectra of 1T-TaSe₂ in the temperature range of 20K to 295K. As the temperature increased, the peaks shifted towards left and the phonon lines got broader.

To further analyze the data, we fit the Raman peaks using curve fitting. Typically, phonon peaks can be fitted with a Lorentz function as follows:

$$y = \frac{a_0}{\pi a_2} \left[1 + \left(\frac{x - a_1}{a_2} \right)^2 \right] \quad (4.4)$$

where a_0 is the amplitude of the peak, a_1 is the center of the peak, a_2 is the width of the peak ($a_2 > 0$). However, if there exists electron-phonon coupling in the sample, the peak becomes asymmetric. In such cases, a Fano function should be used, as shown below,

$$y = \frac{a_0 \left(a_3 + \frac{x - a_1}{a_2} \right)^2}{1 + \left(\frac{x - a_1}{a_2} \right)^2}, \quad (4.5)$$

where a_0 is the amplitude of the peak, a_1 is the center of the peak, a_2 is the width of the peak ($a_2 > 0$), and a_3 is the asymmetry factor [39].

The Voigt function, which is a Lorentz function convoluted by a Gaussian, was chosen to fit the Raman peaks in our experiments and based on the fitting results, the temperature-dependent locations of the peaks and FWHM were determined.

The fitting result is shown in Fig.4.11. First of all, we can clearly see that the phonon energy gradually increases as the temperature decreases. For some phonons, the energy shift is relatively large, e.g., P1, but for high-energy phonons, the dependence of phonon energy on temperature is not immediately

obvious. This is due to the fact that phonons of different energies have different Gruneisen constants and different phonon coupling coefficients, which determine the energy shift of phonons at different temperature [40].

From the fitting curves, it is evident that the line-width of the phonon tends to decrease gradually as the temperature lowers. This is attributed to the lattice contraction described by the constant Gruneisen parameter and anharmonic decay in other phonon modes [40], but for P1 it is an anomaly. One possible reason for this is that because of low Raman shift of P1, its energy value is close to the filter's cut-off frequency and the filter affects the shape of the peaks, which leads to a decrease in line-width with the rising temperature. For the other peaks, especially P5 and P6, their linear relationship is difficult to discern. The reason for this is that perhaps there was too much interference while taking the measurement and the experimental setup was not completely isolated from the external light sources, which may have lead to irregularities in the experiment's results.

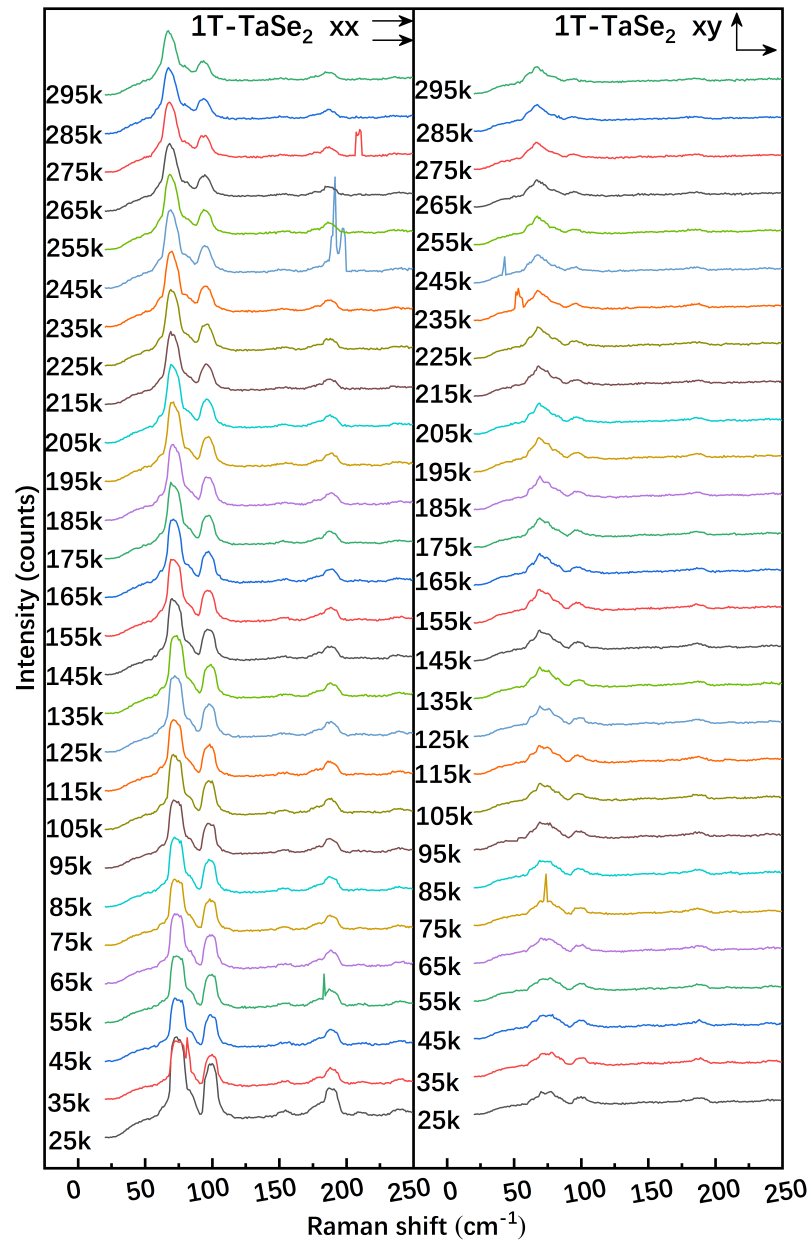


Figure 4.10: The Raman spectra of 1T-TaSe₂. The experiment was started at the temperature of 20K and measurements were carried out with every 5K increase until the temperature of the system reached 295K. The wavelength of the laser light is 531.9 nm.

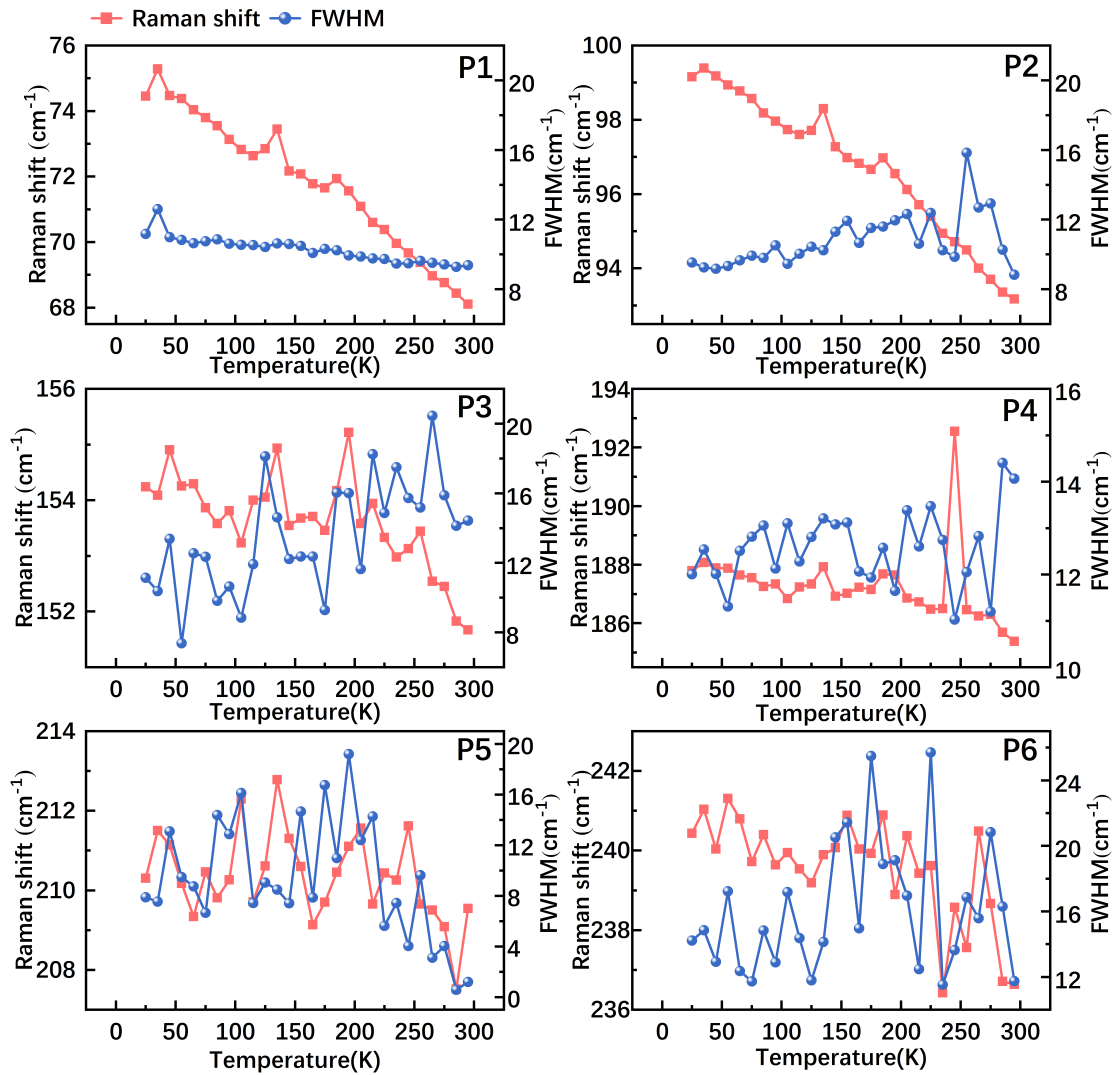


Figure 4.11: Curve fitting result of six Raman peaks in the XX channel. The left axis represents the peak frequency and the right axis represents the line width. The six peaks are labelled as P1 to P6 with the increasing Raman shift, respectively.

5 The upgrade and mounting of the TERS set-up

In this chapter, an upgrade of the TERS system during the research phase based on the original TERS equipment is introduced. During the last three months of the research phase, a small team (Dr. Ge He, Leander Peis and Minghao Zhang) worked on the disassembly of the old system and the integration and installation of a new one. By the end of the project, the equipment was mostly installed, but was still in the process of being tested, therefore there was insufficient time to record measurements using the new TERS system. However, the advantages and improvements brought by the new assembly are still evident.

5.1 The new design and mounting process of TERS set-up

TERS technology has been developed for over twenty years, and there are many applications of it in the analysis of molecular structures, chemical reactions, and more. When a beam of light is focused on the tip, a surface plasma is induced at the apex, creating a strong near field between the tip and the sample surface, therefore the Raman response could be significantly enhanced at this local point. In the previous system, ultra-high vacuum was hard to attain and the tip and sample could not be prepared and transferred in situ, which made the experiments not only more unstable, but difficult to reproduce and time consuming. In addition, when taking TERS measurements, the Ag tip is always recommended to be utilized during the experiment in order to have a strong enhancement effect. However, silver is very easily oxidized in air, which can cause degradation. Therefore, it is necessary to prepare the tips under ultra-high vacuum conditions. Furthermore, an additional chamber for sample cleaning, annealing and cleavage is also required for a better performance of the system. These functions are typically used in the standard STM set-up but their complete integration will greatly improve the TERS measurements. The schematic of the new system is depicted in Fig.5.1, where, in addition to the components of the old set-up, two new chambers were introduced for the in situ preparation. The load lock chamber was for the insertion of sample and tip. In the preparation chamber, a custom made heater and an ion gun for

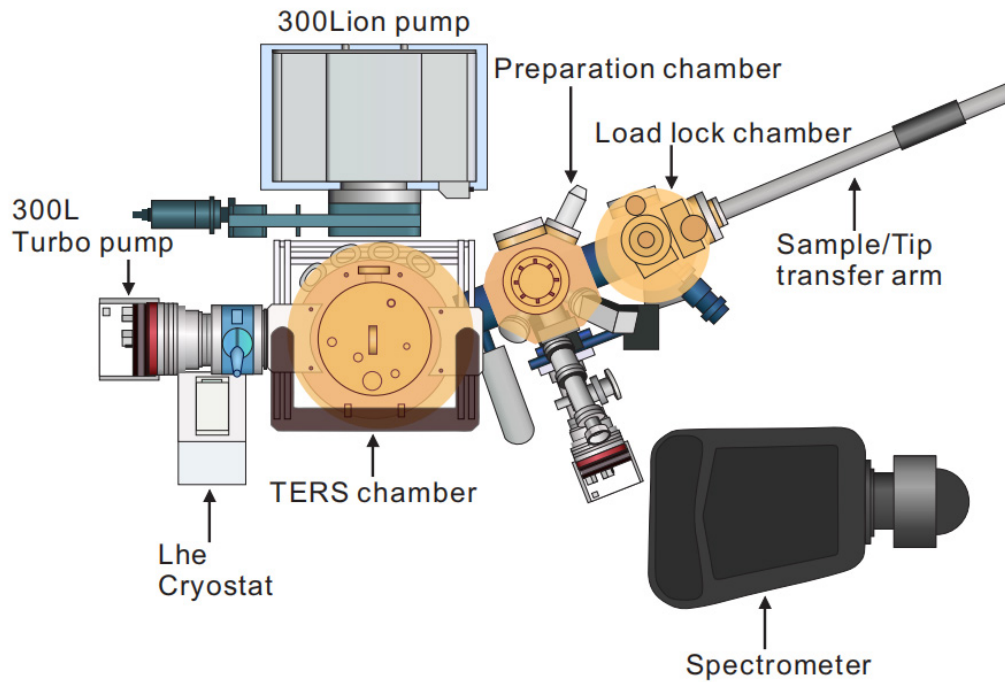


Figure 5.1: The sketch of the new TERS system. The TERS chamber is located in the middle of the system. The preparation chamber, load lock chamber and sample/tip transfer arm are connected to the right side of the TERS chamber sequentially. The ion pump and turbo pump are connected to the back and left side of TERS chamber, respectively. The spectrometer is mounted in the corner of the table.

sample annealing and cleaning were installed. For experimental procedures, the sample or tip is first placed in the load lock chamber and then transferred into the preparation chamber by using the sample transfer arm, whereupon the tip or sample is transferred into the TERS chamber when the preparation process is complete. A closer sketch of the sample/tip transfer system is shown in Fig.5.2. In addition, the TERS chamber and radiation shield were redesigned as well to match the new pumps and sample transfer mechanism.

Before starting the instrument upgrade, the old instrument is demounted. The process of the disassembly of the components was quite fast. Fig.5.3 shows the practical disassembly process during the research phase. The optics, the spectrometer and old TERS chamber were removed sequentially.

During the installation, the vacuum system was firstly upgraded. To begin with, the chambers were installed, into which the pump and tubes were connected, followed by the transfer arm and wobble stick. Then, the sample transfer mechanism was tested under ambient conditions before the entire unit

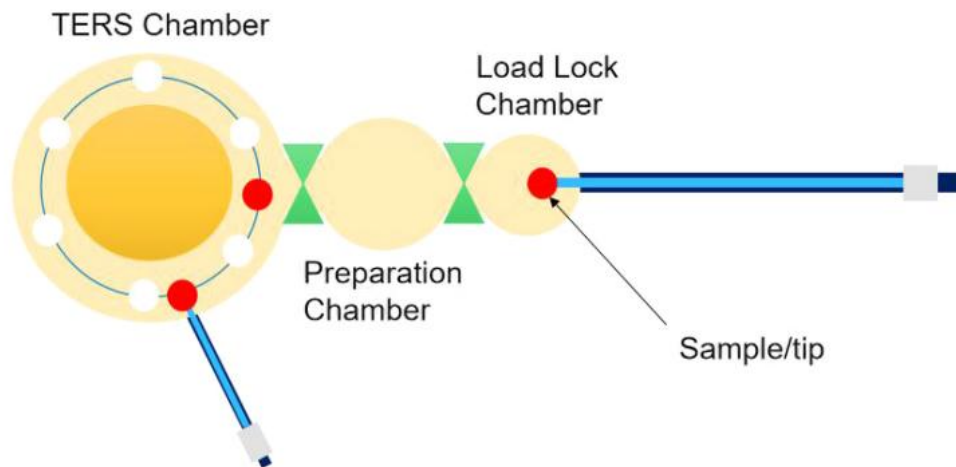


Figure 5.2: The sketch of sample/tip transfer system

was pumped and a leak test was carried out. Finally, the system was baked to a temperature of 80 °C for three days to remove adsorbates on the surface of the vacuum chamber.

After the above components have been mounted, the custom-made heater and Ar ion gun were installed. Fig.5.4 shows the photo of the annealing process with the custom built heater and the ion bombarding process with the Ar ion gun. One of the most important aspects of the new design is the in situ preparation and placement of samples and tips in the preparation chamber. This new design significantly improves the cleanliness of the samples and tips by isolating them from sources of contamination (e.g., air from outside the system).

Remote control of the machine is important, for which a Labview program was developed to help control the sample temperature, and monitor the Helium level in the cryostat and the vacuum in different chambers.

The photo of the Lab before the end of the master thesis can be seen in Fig. 5.5.

5.2 Tests on the new set-up

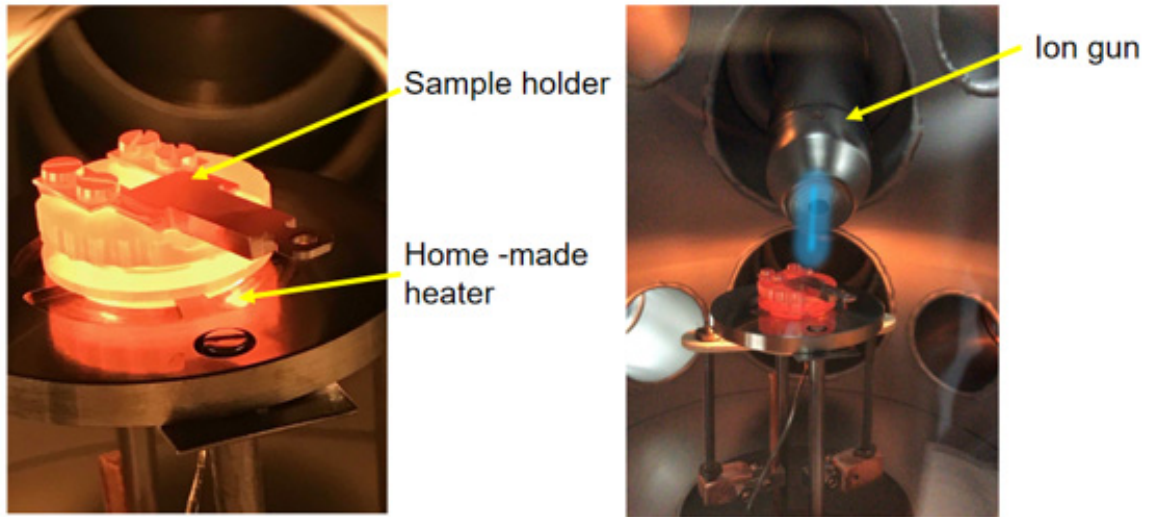
After UHV conditions were achieved, the annealing test was carried out in order to demonstrate that the built-in heater was and is capable of providing enough thermal energy without contaminating the chamber. During the test, the sample holder reached a glowing appearance, indicating that the temperature exceeded 500°C under these conditions, which is normally effective for the annealing. The



Figure 5.3: Photo of the disassembly process

ion gun was then aligned to the sample surface in preparation for the ion bombardment of the sample. In order to check that the ion gun works properly, gold-film was used for the test. After approximately 30 minutes of ion bombardment, it was observed that a portion of the gold was removed, proving that our installation was successful.

Low temperature testing was performed in the last step and after refilling LHe in the system the pressure of the chamber dropped to 9.72×10^{-11} mbar, which is considered as sufficient UHV for experiments herein. The lowest pressure recorded before the upgrade was 1×10^{-8} mbar. In addition, the base temperature, as a contrast to that used in the previous 1T-TaSe₂ Raman measurements, was lowered to 13K. The duration time of the cooling after filling LHe was also reduced, from 8h to 3h.



Preparation Chamber

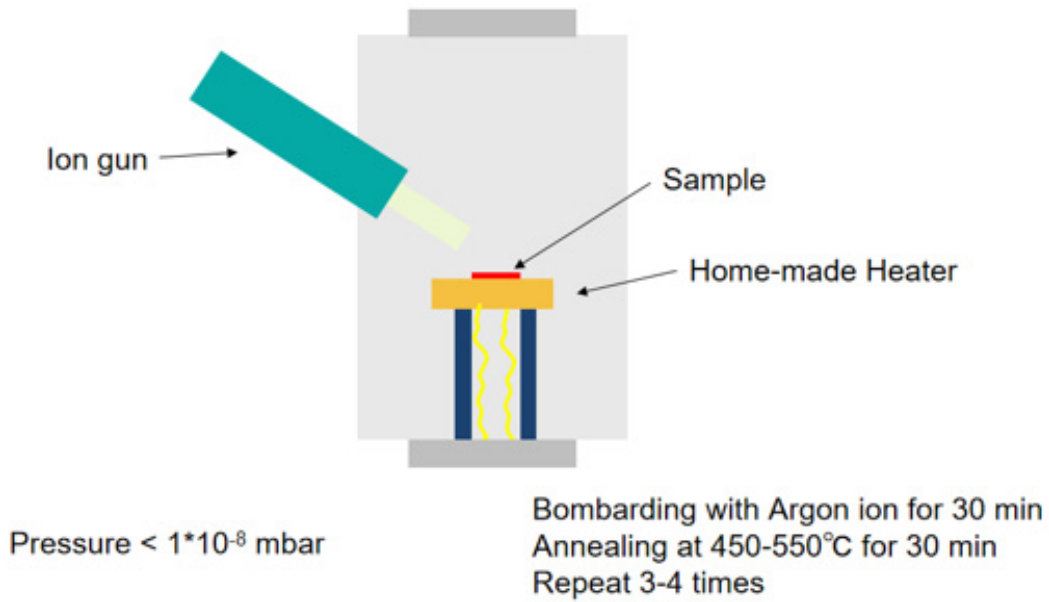


Figure 5.4: Schematic of the annealing process with the custom built heater and the ion bombarding process with an Ar ion gun.

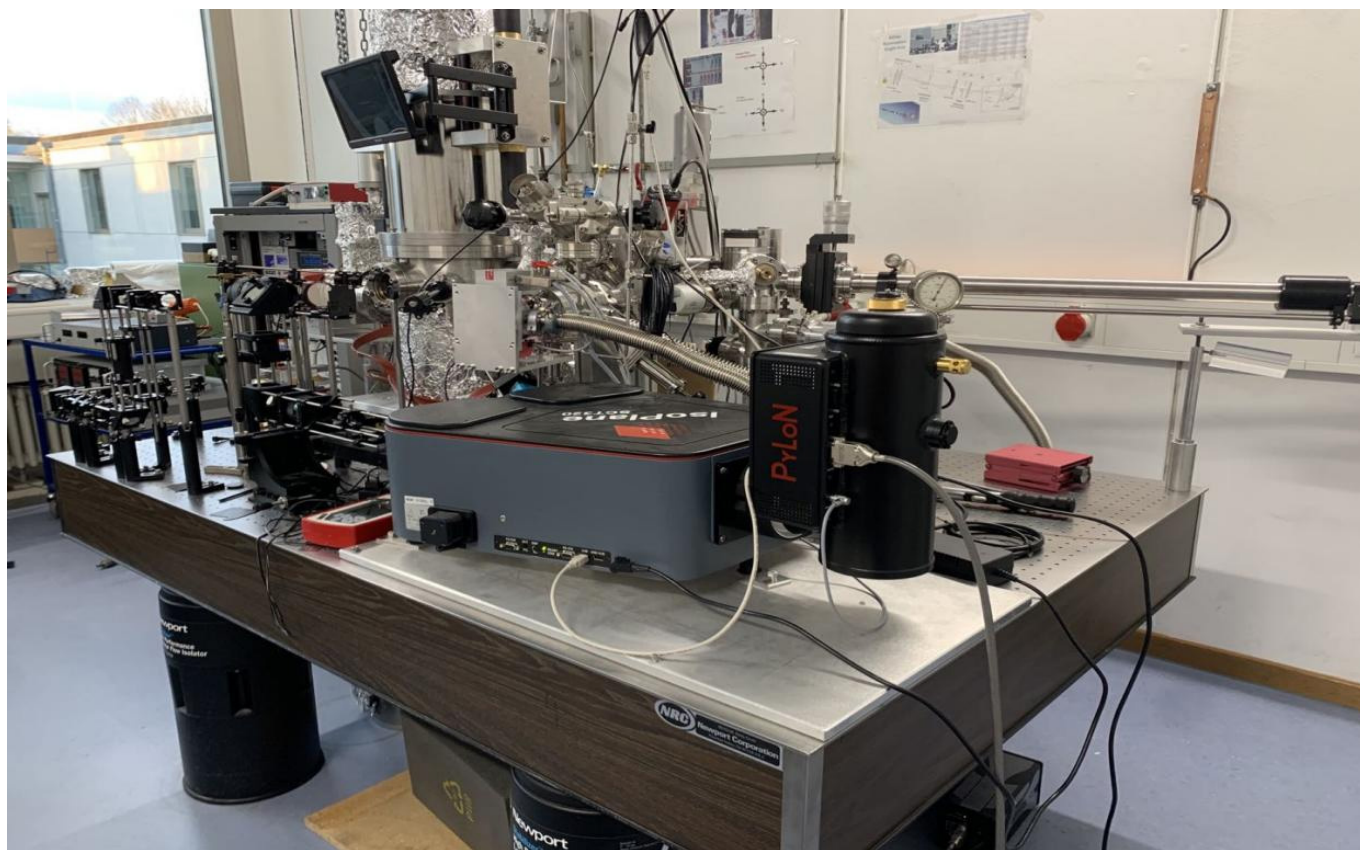


Figure 5.5: The photo of the experimental setup after augmentation.

6 Summary

This thesis investigates the various physical properties of 1T-TaSe₂ through the use of both STM and Raman measurements. STM provides an atomic-level resolution and can clearly demonstrate the topography and information on the electronic density of states on the surface of 1T-TaSe₂ under CDW distortion. With the help of Raman spectroscopy, the characteristic spectral features of 1T-TaSe₂ can be obtained. By combining the two techniques, topographic and spectroscopic information and single- and two-particle properties are obtained simultaneously. If tip-enhanced Raman spectroscopy (TERS) can be used, the resolution of ordered domains may become possible.

Extensive Raman measurements of 1T-TaSe₂ were carried out and phonon lines were obtained in the XX and XY polarization configurations from low (20K) to room temperature (295K). For XX polarisation, phonon Raman peaks in the range of 150 cm⁻¹ to 250 cm⁻¹ were observed, as well as lines from phonons with Raman shifts of less than 100 cm⁻¹. For XY configuration, no peaks different from those XX polarization were observed. One possible reason for this was that the photon polarization was changed by the parabolic mirror.

For the STM experiment on 1T-TaSe₂, the expected resolution could not be obtained and no superlattice structure was seen. Presumably, the contamination with adsorbates reduced the expected resolution since neither the sample nor the scanning tip could be handled in situ.

To overcome these issues, the experimental equipment was upgraded during the thesis work. Two new chambers were introduced into the system for the in-situ preparation and the TERS chamber was also modified. These augmentations allowed the samples to be cleaved and annealed within the system and transferring them without breaking the vacuum.

Vacuum and tests at low temperature were carried out on the new equipment, and the vacuum level that could be achieved was decreased by almost two orders of magnitude compared to the machine before upgrading. The minimal pressure was observed to be 9.72×10^{-11} mbar. For time limitations it was not possible to redo the experiments under UHV conditions. Nevertheless, the new equipment

is expected to facilitate better resolutions and stability.

7 Bibliography

- [1] **Alpichshev.Z, Analytis.J.G, Chu.J.H, et al.** *STM imaging of electronic waves on the surface of Bi_2Te_3 : topologically protected surface states and hexagonal warping effects*[J]. Physical review letters, 2010, 104(1): 016401.
- [2] **Hapala.P, Kichin.G, Wagner.C, et al.** *Mechanism of high-resolution STM/AFM imaging with functionalized tips*[J]. Physical Review B, 2014, 90(8): 085421.
- [3] **Kordyuk.A.A.** *ARPES experiment in fermiology of quasi-2D metals*[J]. Low Temperature Physics, 2014, 40(4): 286-296.
- [4] **Naish.V.E, Ozerov.R.P.** *Neutron diffraction of magnetic materials*[M]. Springer Science & Business Media, 2012.
- [5] **Monshi.A, Foroughi.M.R, Monshi.M.R.** *Modified Scherrer equation to estimate more accurately nano-crystallite size using XRD*[J]. World journal of nano science and engineering, 2012, 2(3): 154-160.
- [6] **Rygula.A, Majzner.K, Marzec.K.M, et al.** *Raman spectroscopy of proteins: a review*[J]. Journal of Raman Spectroscopy, 2013, 44(8): 1061-1076.
- [7] **Baker.M.L, Mara.M.W, Yan.J.J, et al.** *K-and L-edge X-ray absorption spectroscopy (XAS) and resonant inelastic X-ray scattering (RIXS) determination of differential orbital covalency (DOC) of transition metal sites*[J]. Coordination chemistry reviews, 2017, 345: 182-208.
- [8] **Binnig G, Rohrer H, Gerber C, et al.** *Surface studies by scanning tunneling microscopy*[J]. Physical review letters, 1982, 49(1): 57.
- [9] **Baratoff.A.** *1986 Nobel Prizes Development of Scanning Tunnelling Microscopy*[J]. Europhysics News, 1986, 17(11-12): 141-144.

- [10] URL:https://en.wikipedia.org/wiki/Scanning_probe_microscopy, (2021).
- [11] **Raman.C.V, Krishnan.K.S.** *A new type of secondary radiation*[J]. Nature, 1928, 121(3048): 501-502.
- [12] **Landsberg.G, Mandelstam.L.** *A novel effect of light scattering in crystals*[J]. Naturwissenschaften, 1928, 16(5): 5.
- [13] **H.M. Eiter.** *Master's thesis.* Technische Universität München, (2008).
- [14] **X.J.Fang, D.Lu.** *Solid state physics.* Shanghai Scientific & Technical Publishers, (1980).
- [15] **Tsang.J.C, Smith.Jr.J.E, Shafer.M.W, et al.** *Raman spectroscopy of the charge-density-wave state in 1T-and 2H-TaSe₂.*[J]. Physical Review B, 1977, 16(10): 4239.
- [16] **Hossain.M, Zhao.Z, Wen.W, et al.** *Recent advances in two-dimensional materials with charge density waves: synthesis, characterization and applications*[J]. Crystals, 2017, 7(10): 298.
- [17] **Chen.Y, Ruan.W, Wu.M, et al.** *Strong correlations and orbital texture in single-layer 1T-TaSe₂*[J]. Nature Physics, 2020, 16(2): 218-224.
- [18] **Wilson.J.A, Di.Salvo.F.J, Mahajan.S.** *Charge-density waves in metallic, layered, transition-metal dichalcogenides*[J]. Physical review letters, 1974, 32(16): 882.
- [19] **Eibschutz.M.** *Sign and amplitude of commensurate charge-density waves in 1T-TaSe₂*[J]. Physical Review B, 1992, 45(19): 10914.
- [20] **G.He.** *Private communication.*
- [21] **K.Huang.** *Solid State Physics.* Beijing, Higher Education Press, (1988).
- [22] **X.Y.Hou.** *Scanning Tunneling Microscopy / Spectroscopy of Transition Metal Dichalcogenides. Doctoral Dissertation.* Institute of Physics, Chinese Academy of Science, (2017).
- [23] **Z.Q.LI.** *The survey and token of micro-scale surface. Master's thesis.* China, Chongqing university, (2006).

- [24] **L.M.Yan.** *The Study of the Physical Properties of Transition Metal Diselenides Synthesized by High Pressure and High Temperature. Master's thesis.* Jilin University, (2018).
- [25] **Fischer.O, Kugler.M, Maggio-Aprile.I, et al.** *Scanning tunneling spectroscopy of high-temperature superconductors[J].* Reviews of Modern Physics, 2007, 79(1): 353.
- [26] **N.Chelwani.** *Dissertation.* Technische Universität München, (2018).
- [27] **G.Z.Wu.** *Raman spectroscopy.* Beijing, Science Press, (2007).
- [28] **R.Hosseinian.** *Master's Thesis.* Technische Universität München, (2016).
- [29] **J-R.Scholz.** *Master's Thesis.* Technische Universität München, (2017).
- [30] **D.Hoch.** *Master's Thesis.* Technische Universität München, (2015).
- [31] **P.Cova.** *Bachelor's thesis.* Technische Universität München, (2017).
- [32] **Chaika.A.N, Orlova.N.N, Semenov.V.N, et al.** *Fabrication of [001]-oriented tungsten tips for high resolution scanning tunneling microscopy[J].* Scientific reports, 2014, 4(1): 1-6.
- [33] *URL:https://baike.baidu.com/item/%E6%89%AB%E6%8F%8F%E9%9A%A7%E9%81%93%E6%98%BE%E5%BE%AE%E9%95%9C/6927647?fromtitle=STM&fromid=1027292&fr=aladdin,* (2021).
- [34] **S.L.Zhang.** *The scientific and technical basis of Raman spectroscopy and its construction and application.* Beijing, Peking University Press, (2020).
- [35] *URL:https://www.cryst.ehu.es.*
- [36] **Samnakay.R, Wickramaratne.D, Pope.T.R, et al.** *Zone-folded phonons and the Commensurate-Incommensurate Charge-Density-Wave Transition in 1T-TaSe₂ Thin Films[J].* Nano letters, 2015, 15(5): 2965-2973.
- [37] **Sun.S, Wei.L, Li.Z, et al.** *Direct observation of an optically induced charge density wave transition in 1T-TaSe₂[J].* Physical review B, 2015, 92(22): 224303.

- [38] **Yan.J.A, Cruz.M.A.D, Cook.B, et al.** *Structural, electronic and vibrational properties of few-layer 2H-and 1T-TaSe₂[J]*. Scientific reports, 2015, 5(1): 1-13.
- [39] **J.W.Zhang.** *Origin 9.0 The Manual of Scientific and Technical Mapping and Data Analysis.* China, Posts And Telecom Press,(2014).
- [40] **Baum.A, Milosavljevic.A, Lazarevic.N, et al.** *Phonon anomalies in FeS[J]*. Physical Review B, 2018, 97(5): 054306.

8 Acknowledgement

Upon the completion of this thesis, I am grateful to those who have offered me encouragement and support during the course of my study. Particularly, I would like to thank

Prof. Dr. Rudolf Gross for giving me the opportunity to work at the Walther Meissner-Institut.

Prof. Dr. Rudi Hackl, my supervisor, who has offered me numerous valuable comments, incomparable patience and understanding during the completion of my Master's Thesis.

Dr. Ge He for his constant encouragement and guidance. Without his consistent and illuminating instruction, this thesis could not have reached its present form.

Dr. Andreas Baum and **Leander Peis** for all their help and the productive discussions.

The **technical staff** for manufacturing many of the parts needed for the setup.

Finally, I am very grateful to **my parents**. Only with their selfless support, concern and love, can I overcome those difficulties and pursue my study till now. Their loving considerations and helps are the source of my strength.